CHAPTER VI

OBSERVATIONS

To demonstrate the viability of LMTs for scientific research, a variety of images acquired with the NASA-LMT are presented along with sample results from both the orbital object and astronomical observing programs.

A. Orbital Object Observations and Sample Results

As introduced in Chapter II, the NASA-LMT was primarily developed to study the population of orbital objects in order to characterize the properties of the orbital environment and provide a more accurate collisional risk assessment for space-faring activities. Optical observations can be used to investigate the physical properties of individual objects such as material construction and albedo, or the statistical properties of the overall population such as the determination of the distribution function.

Initially, data were acquired with a CCD in drift-matching (DM) mode in order to enhance the detection of faint objects by maximizing the SN ratio for objects detected at a specific altitude and inclination. Because of the high selectiveness of DM mode, however, it is best applied to the study (eg. albedos, phase functions) of catalogued objects where the orbital elements are already known, rather than in the detection of new objects in a blind-staring mode where the detection rate is poor. To reduce selectiveness and thereby enhance the detection rate, DM mode observations were supplanted after

the first 6 months of operations with a sidereally drift-scanning CCD coupled to a rotating beam chopper located near the focal plane. Despite the loss of sensitivity due to the excess accumulation of background light after object passage, the detection rate improved relative to DM mode because of the broader altitude and inclination window. The chopper enabled the determination of altitude via object angular rate under the circular orbit assumption and, because it was asymmetrical, the object direction of motion as well. Although the sidereal mode detection rate improved relative to DM mode by an order of magnitude to a few events per hour, the sensitivity unfortunately declined from a DM mode detection capability of ~2 cm diameter (0.1 albedo specular sphere @ 1000 km) to ~20 cm. The LMTs primary mission to observe orbital objects in the 1 to10 cm diameter size regime was thus unfulfilled and its contribution to an understanding of the orbital environment was limited.

The introduction of a MCP intensified video camera at the beginning of the second year of NODO operations solved the dilemma by providing a detector with moderate sensitivity and a high frame rate. The MCP based camera was similar to the sidereal mode CCD in its lack of selectiveness and thus broad acceptance of object altitude and inclination. Unlike the poor sensitivity of the slow scanning sidereal mode CCD however, the 30 frame per second video frame rate of the MCP based camera essentially eliminated the problem of SN ratio reduction from excess background accumulation because the field crossing time is more closely matched to the frame rate. MCP based cameras completely replaced CCDs at NODO for the acquisition of orbital object data after successful initial trials in 1996. Figures VI.A-1 through 10 illustrate

NASA-LMT: Orbital Object Detection via CCD Drift-Matching Mode

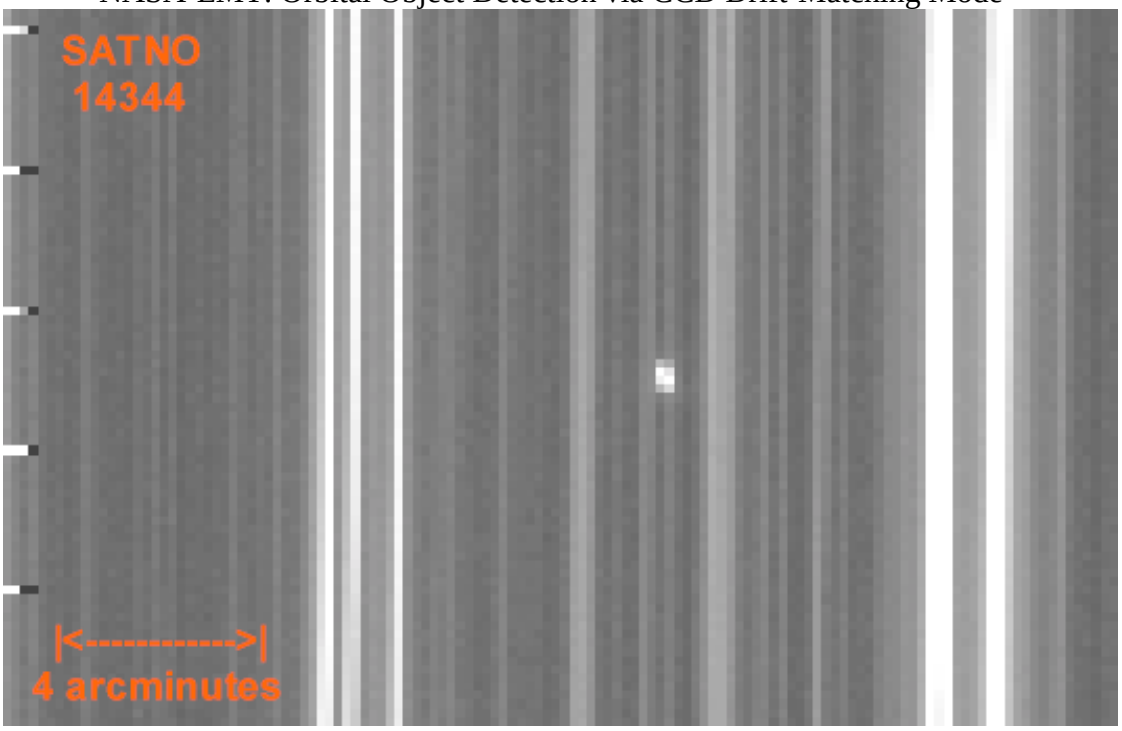

Figure VI.A-1. A demonstration of the detection of an orbiting object via the drift-matching (DM) mode of CCD operation. The CCD has been set such that its read direction and read rate exactly match the orbital parameters of a catalogued object. In this example, the object is Satellite Number 14344 which is a piece of SL-8 debris with a RCS derived diameter of 12.5 cm. When crossing through the LMT FOV, the object was at an altitude of 775 km with an angular velocity of 0.5833 degrees/sec, a position angle of motion of 74 degrees and a solar phase angle of 68 degrees. The CCD was oriented accordingly and then read at the corresponding rate. The object signal photons were then able to accumulate on only several pixels rather than streak through the FOV. The vertical streaks are background stars which are virtually stationary at this high read rate and short effective exposure time of 0.585 seconds. Based upon the measured net flux above background (1900 ADU) coupled with the assumption of a 0.1 albedo and a specular phase function, the object optical cross-section (OCS) based diameter is approximately 5.12 cm. This white light image was acquired with the LSP 2K CCD with 16x16 binning in order to accommodate the high angular rate and consequent short readout time.

NASA-LMT: Orbital Object Detection via CCD Drift-Matching Mode

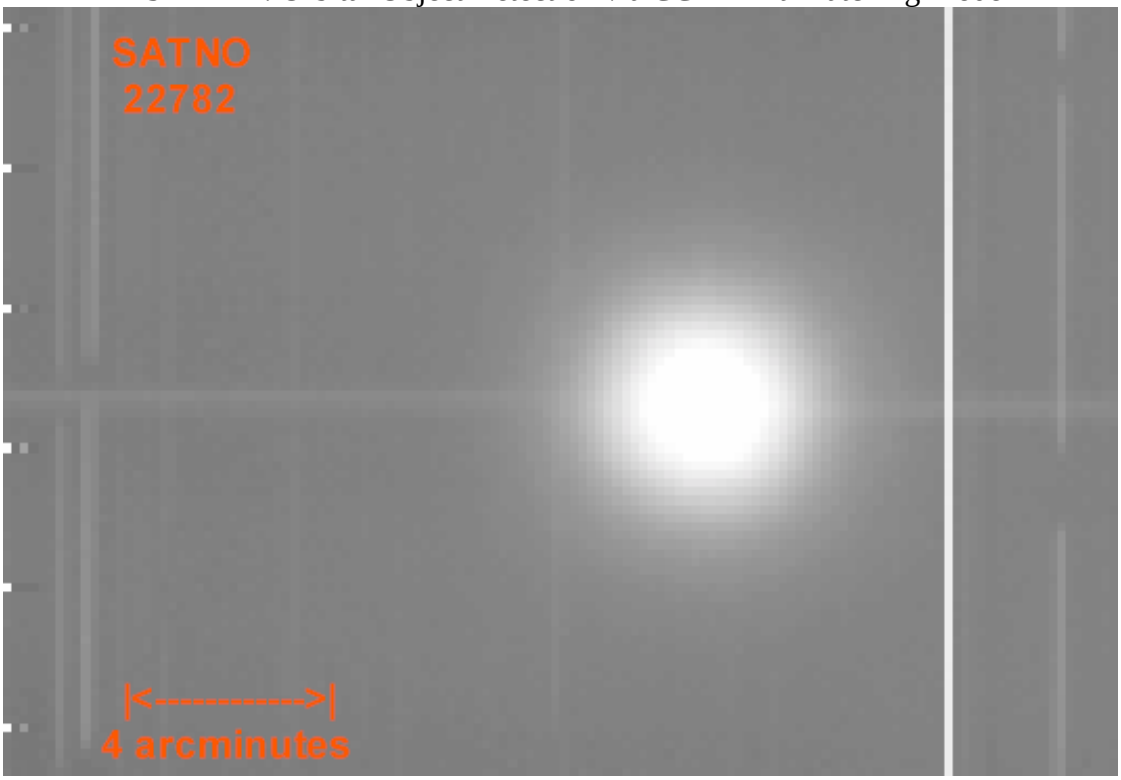

Figure VI.A-2. A demonstration of the detection of an orbiting object via the drift-matching mode of CCD operation. The CCD has been set such that its read direction and read rate exactly match the orbital parameters of a catalogued object. In this example, the object is Satellite Number 22782 which is a piece of Meteor 2-21 debris with a RCS derived diameter of 6.28 m. When crossing through the LMT FOV, the object was at an altitude of 949 km with an angular velocity of 0.446 degrees/sec, a position angle of motion of 265 degrees and a solar phase angle of 69 degrees. The CCD was oriented accordingly and then read at the corresponding rate. The object signal photons were then able to accumulate on only several pixels, neglecting the obvious saturation, rather than streak through the FOV. The vertical streaks are background stars which are virtually stationary at this high read rate and short effective exposure time of 0.765 seconds. Based upon the approximate net flux above background of 2.5 million ADU (compensating for the saturation), coupled with the assumption of a 0.1 albedo and a specular phase function, the object optical cross-section (OCS) based diameter is approximately 2.02 m. This white light image was acquired with the LSP 2K CCD with 16x16 binning in order to accommodate the high angular rate and consequent short readout time.

NASA-LMT: Orbital Object Detection via CCD Drift-Matching Mode

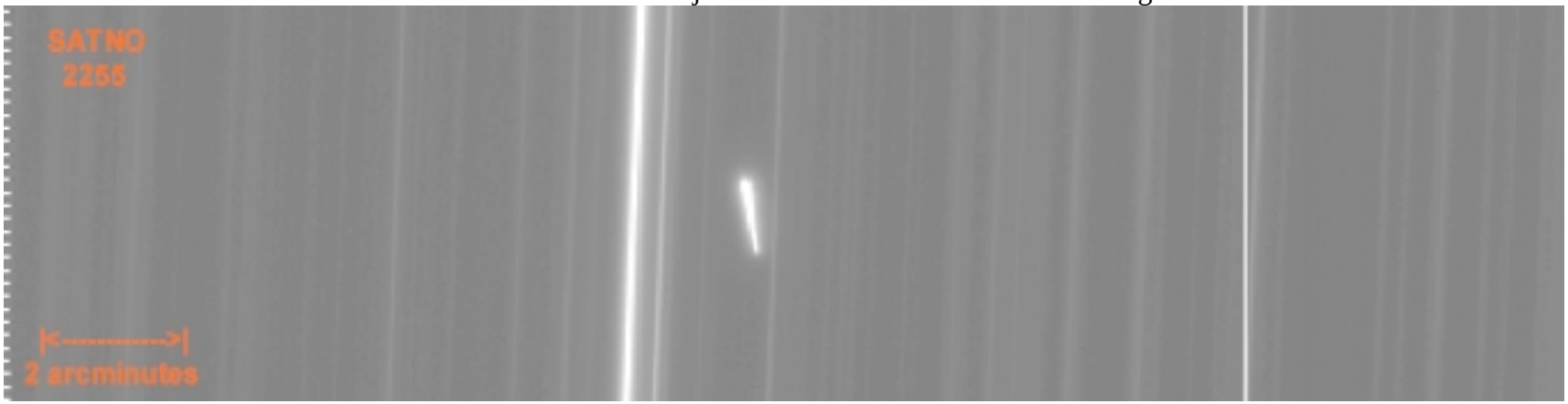

Figure VI.A-3. A demonstration of the detection of an orbiting object via the drift-matching (DM) mode wherein the CCD angular rate and position angle do not exactly match the object's motion. In this example, the object is Satellite Number 2255 which is a piece of Thorad Agena debris with a RCS derived diameter of 2.64 m. When crossing through the LMT FOV, the object was at an altitude of 4233 km with an angular velocity of 0.082 degrees/sec, a position angle of motion of 272 degrees and a solar phase angle of 69 degrees. Given the image angle and elongation, the CCD position angle and read rate were incorrect by approximately 8 degrees and 4.9% respectively. The vertical streaks are background stars which are virtually stationary at this high read rate and short effective exposure time of 4.11 seconds. Based upon the measured net flux above background (144,000 ADU) coupled with the assumption of a 0.1 albedo and a specular phase function, the object optical-cross section (OCS) based diameter is approximately 91.8 cm. This white light image was acquired with the LSP 2K CCD with 4x4 binning in order to accommodate the moderate angular rate and readout time.

NASA-LMT: Orbital Object Detection via CCD Drift-Matching Mode

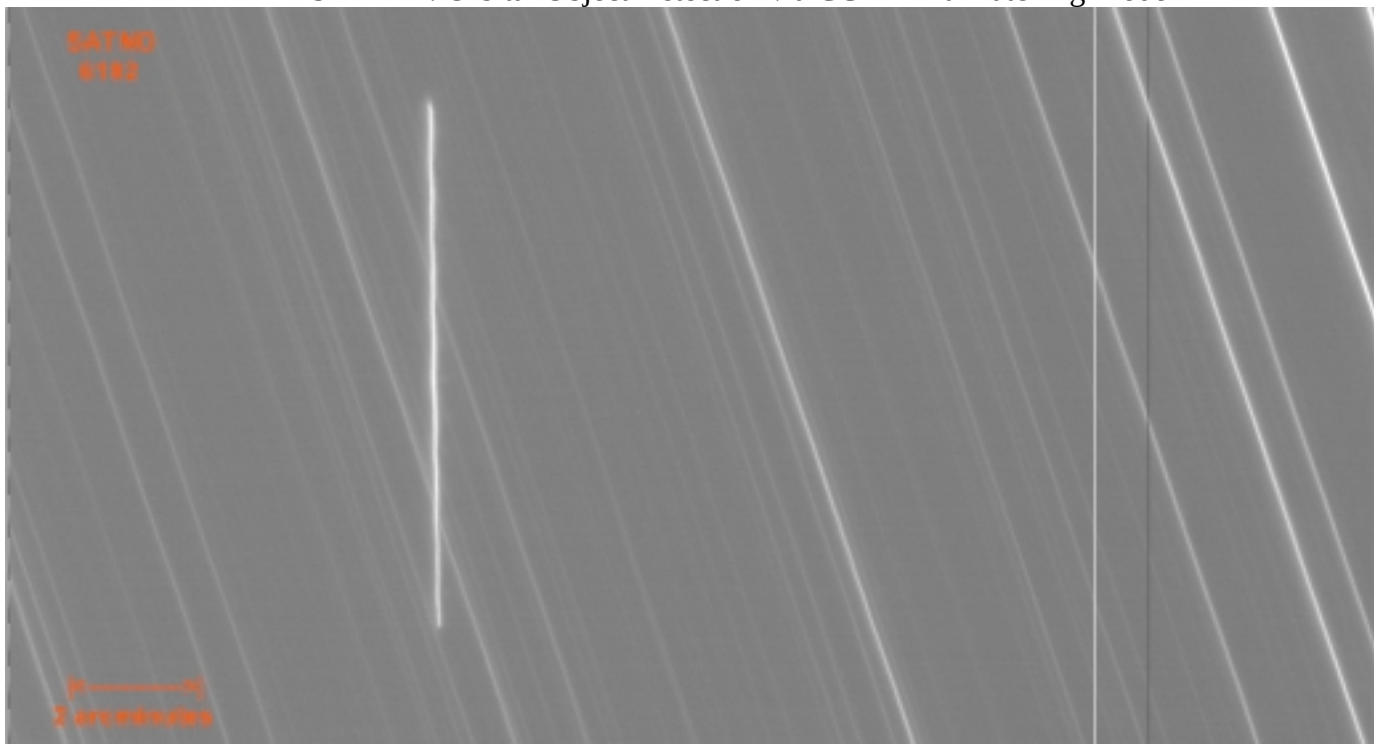

Figure VI.A-4. A demonstration of the detection of an orbiting object via the drift-matching mode (DM) wherein the CCD read rate is incorrect. In this example, the object is Satellite Number 6192 which is a piece of Cosmos 520 debris with a RCS derived diameter of 3.05 m. When crossing through the LMT FOV, the object was at an altitude of 20,655 km with an angular velocity of 0.0206 degrees/sec, a position angle of motion of 262 degrees and a solar phase angle of 44 degrees. The CCD position angle orientation was correct, but the read rate was incorrect by 38%. The object signal photons thus spread along the CCD read direction (columnar). The tilted streaks are background stars which drifted sidereally (east-west) during this relatively long 16.57 seconds scan. Based upon the net measured flux above background (390,00 ADU), coupled with the assumption of a 0.1 albedo and a specular phase function, the object OCS based diameter is approximately 3.67 m. This white light image was acquired with the LSP 2K CCD with 2x2 binning in order to accommodate the moderate angular rate and readout time.

NASA-LMT: Orbital Object Detection via CCD Drift-Matching Mode

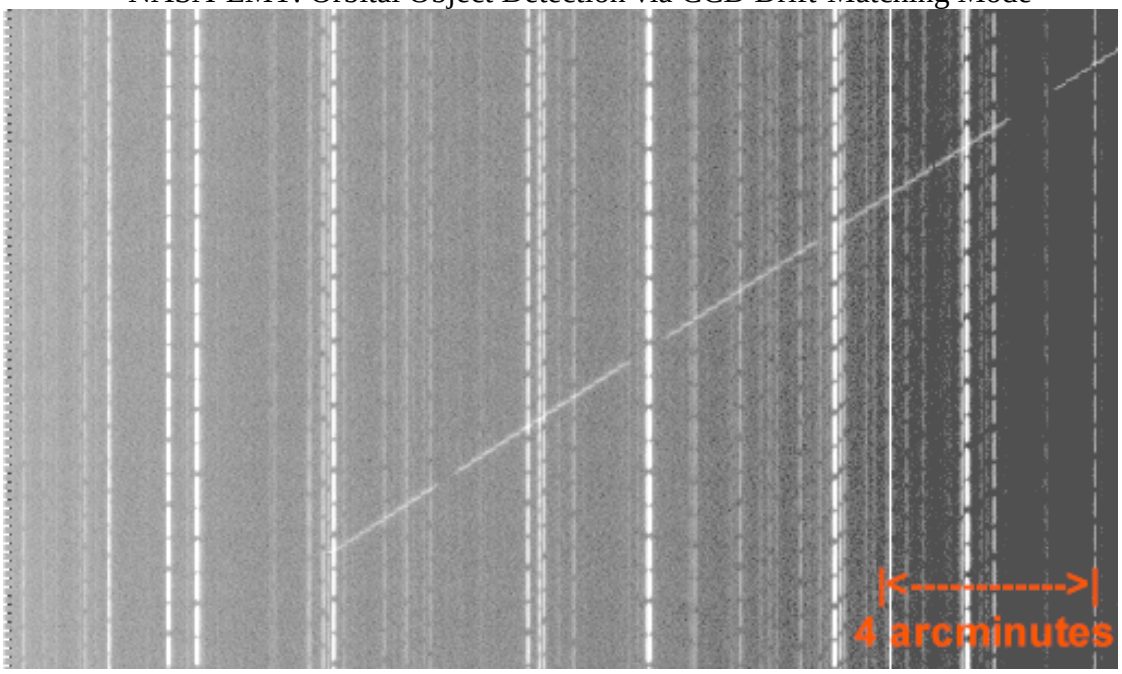

Figure VI.A-5. A demonstration of the detection of a random object via the drift-matching (DM) mode of CCD operation. The CCD read direction and read rate are set to search an arbitrary orbital inclination and altitude. The rotating beam chopper is operating so that the angular velocity and direction of a detected orbital object can be measured. In this example, the object is an uncorrelated (un-catalogued) object moving relative to the CCD scan which was set to search a 930 km altitude (0.455 degrees/sec) and 295 degree position angle. The chopper was rotating at 60 Hz, implying an object exposure of 0.0667 seconds and an angular velocity of 4.28 degrees/sec (based on four demarcations (chops) in the 428 pixel object trail and a plate scale of 2.4 arcseconds/pixel). The object is therefore a meteor because a bound orbit with such a high angular rate would have a perigee deep within the earth's atmosphere. The vertical streaks are background stars which are virtually stationary at this high read rate and short effective exposure time of 0.750 seconds for the stars. Based upon the measured flux above background of 8,132 ADU, the meteor apparent magnitude is approximately 12.10. This white light image was acquired with the LSP 2K CCD with 4x4 binning in order to accommodate the moderate angular rate and readout time for this random search.

NASA-CCD Debris Telescope: Orbital Object Detection via CCD DM Mode

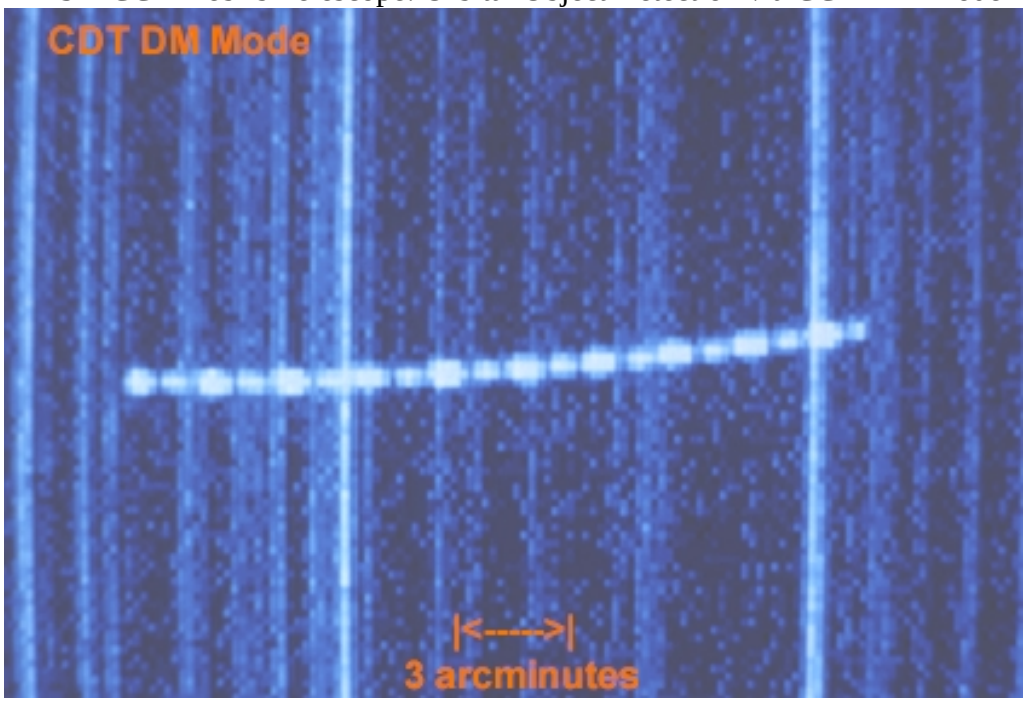

Figure VI.A-6. A NASA-CDT Image. A demonstration of the detection of an orbiting object via the drift-matching (DM) mode wherein the CCD read direction is intentionally offset from the object's position angle of motion in order to provide time resolution. This example was not acquired with the NASA-LMT, but is included to demonstrate a tumbling object acquired in the DM mode. By offsetting the CCD read direction, the object drifts across the CCD orthogonal to the read direction rather than concentrating on a few pixels. For objects with time varying intensity, this can be a useful way to study object shapes and still retain the relatively high sensitivity of the DM technique. This object appears to alternately present two different reflective surfaces to the telescope. This white light image was acquired with the NASA CCD Debris Telescope (CDT) equipped with a Fairchild 384x576 CCD with 23 um pixels and a 11.25 arcsecond/pixel plate scale. The CDT was described briefly in Chapter II.

NASA-LMT: Orbital Object Detection via CCD Sidereal Drift-scanning Mode

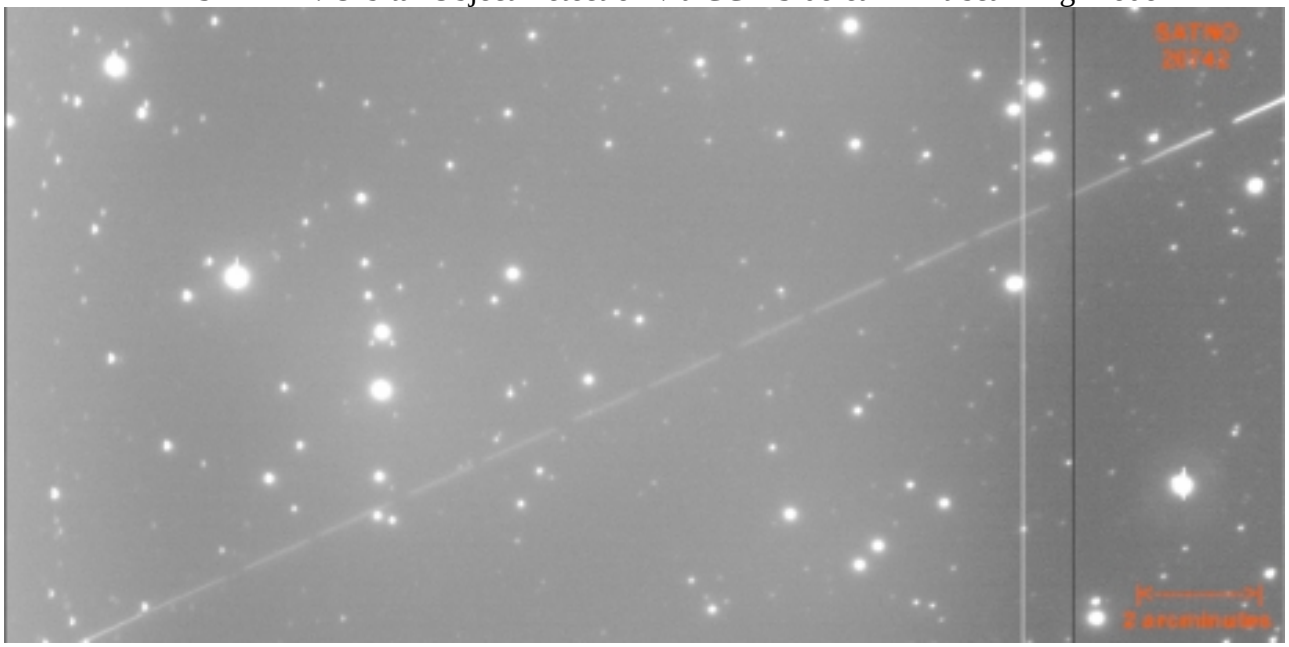

Figure VI.A-7. The detection of an orbiting object via the sidereal mode of CCD operation. The CCD has been set such that its read direction and read rate exactly match the sidereal drift. A rotating asymmetrical beam chopper is used so that the angular rate and direction may be determined for any object passing through the FOV. The fixed rotation rate yields either the object field crossing time or segments of known duration, and the blade asymmetry yields a deterministic pattern to the streak segments and gaps (long and short) to yield direction of motion. In this example, the object is Satellite Number 20472 which is an operational Russian Molniya communications satellite (#1-78) in a highly elliptical orbit with a RCS diameter of 4.45 m. The object was at an altitude of 13,054 km with an angular velocity of 0.0388 degrees/sec, a position angle of motion of 102 degrees, and a solar phase angle of only 36 degrees. Since the CCD was sidereal drift-scanning, the object signal photons were spread over the detector as it passed through the FOV, rather than concentrated on several pixels as with DM mode. The object exposure was 7.29 seconds based on its angular rate and trail length, whereas the field exposure was 97 seconds. The excess background exposure and image spread contribute to a significant reduction in SN ratio and thus a loss in sensitivity relative to DM mode detections. Based upon the estimated flux above background (127,000 ADU), coupled with the assumption of a 0.1 albedo and a specular phase function, the object OCS based diameter is 2.00 m. This white light image was acquired with the LSP 2K CCD with 1x1 binning.

NASA-LMT: Video Images of a Satellite Transit

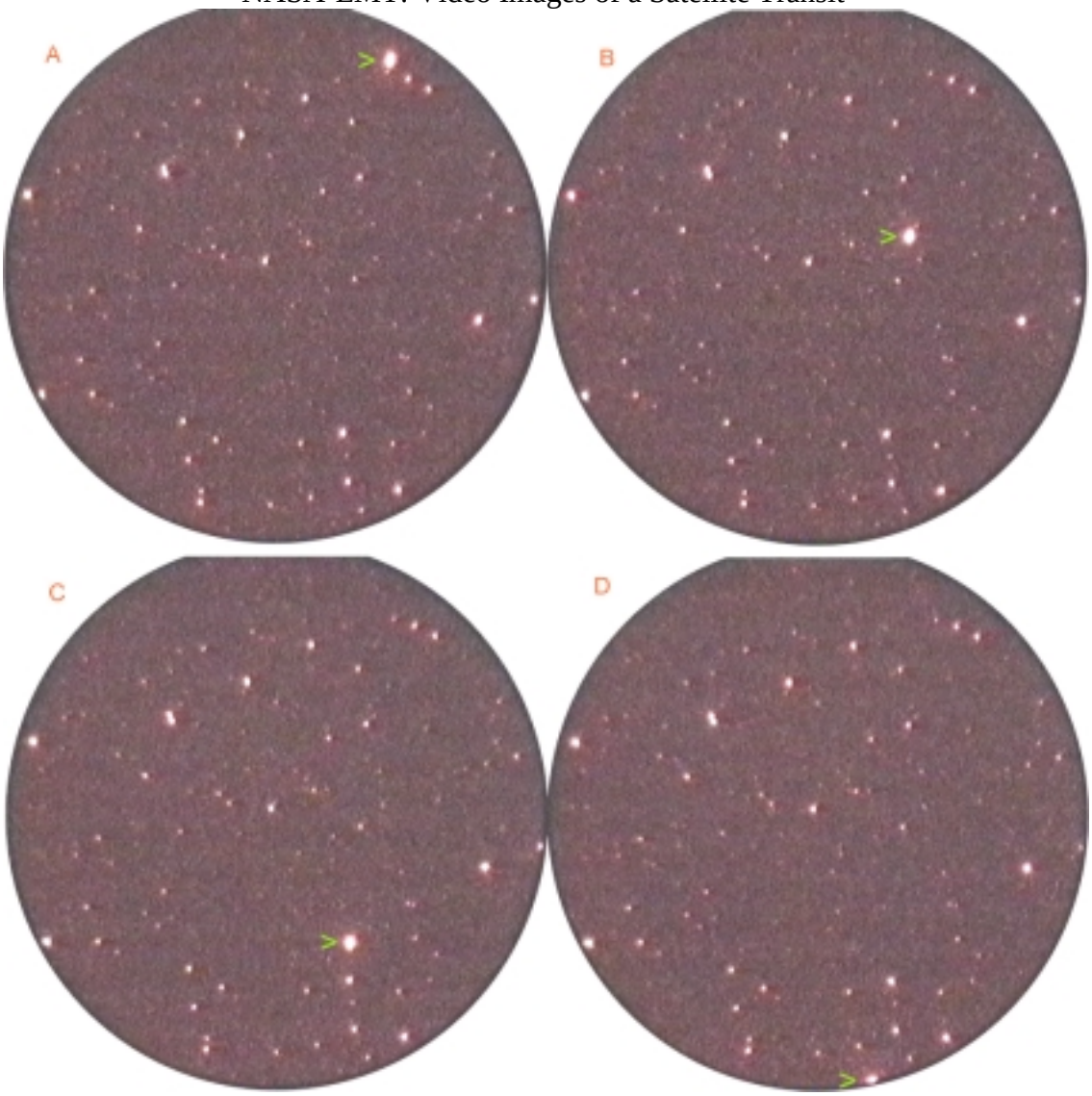

Figure VI.A-8. Time series of white light video images acquired with the NASA-LMT using the 40mm 2nd generation Micro-Channel Plate (MCP) intensified digital video camera. The field of view is 0.444 degrees in diameter. The interval between frames is 0.167 seconds which yields an angular velocity for the object (indicated by green arrow) of approximately 0.813 degrees/sec. Assuming the object is in a circular orbit, this corresponds to an altitude of 535 km. By calibrating the image using field stars of known brightness and assuming an albedo and phase function, the object size can be obtained. In this example, the apparent magnitude is approximately 11 which when coupled with the assumption of a 0.1 albedo and a specular phase function, yields an object OCS based diameter of approximately 19 cm. The limiting apparent magnitude with this detector is approximately 16.5.

NASA-LMT: Video Images of a Tumbling Orbital Object

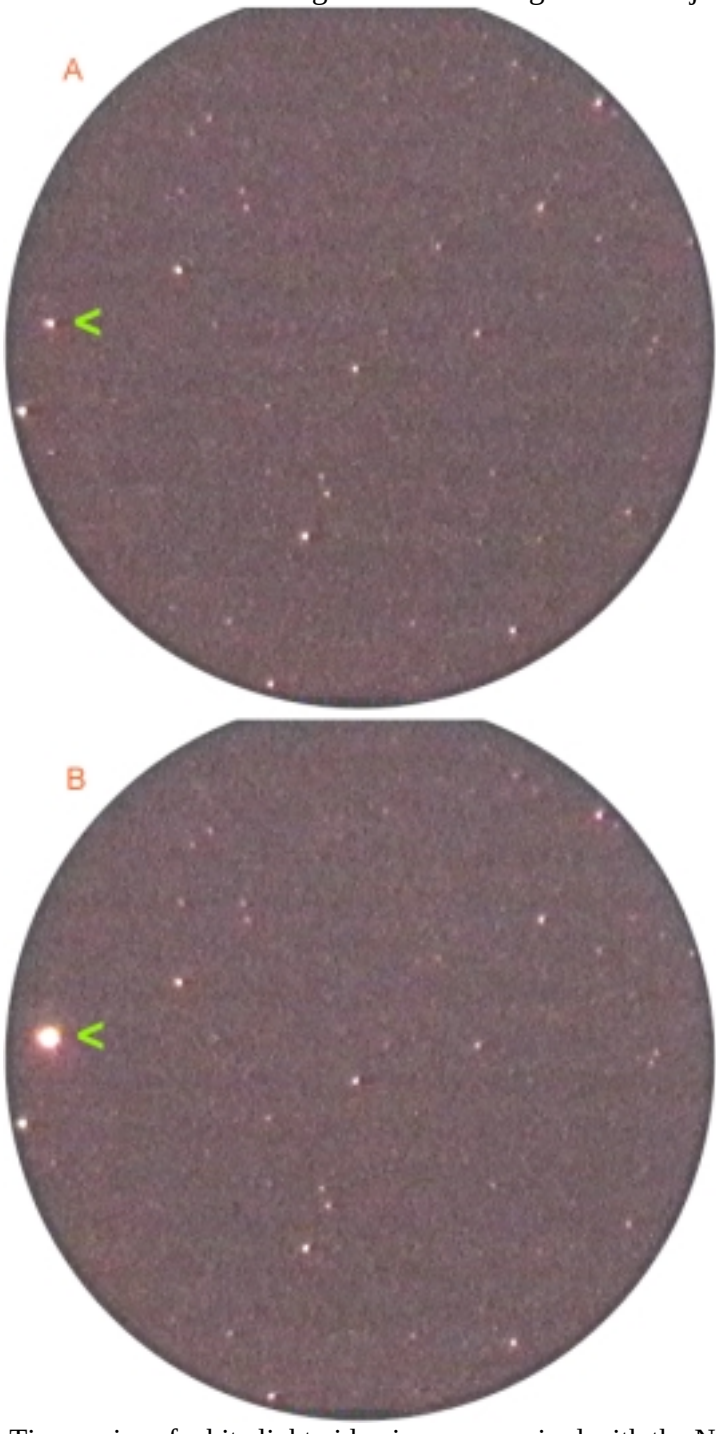

Figure IV.A-9. Time series of white light video images acquired with the NASA-LMT using the 40mm 2nd generation Micro-Channel Plate (MCP) intensified digital video camera. The field of view is 0.444 degrees in diameter and the interval between frames is 0.033 seconds. This is an image of a rotating object which when oriented appropriately yields a specular reflection of the sun. The limiting apparent magnitude with this detector is approximately 16.5.

NASA-LMT: Video Images of a Meteor Event

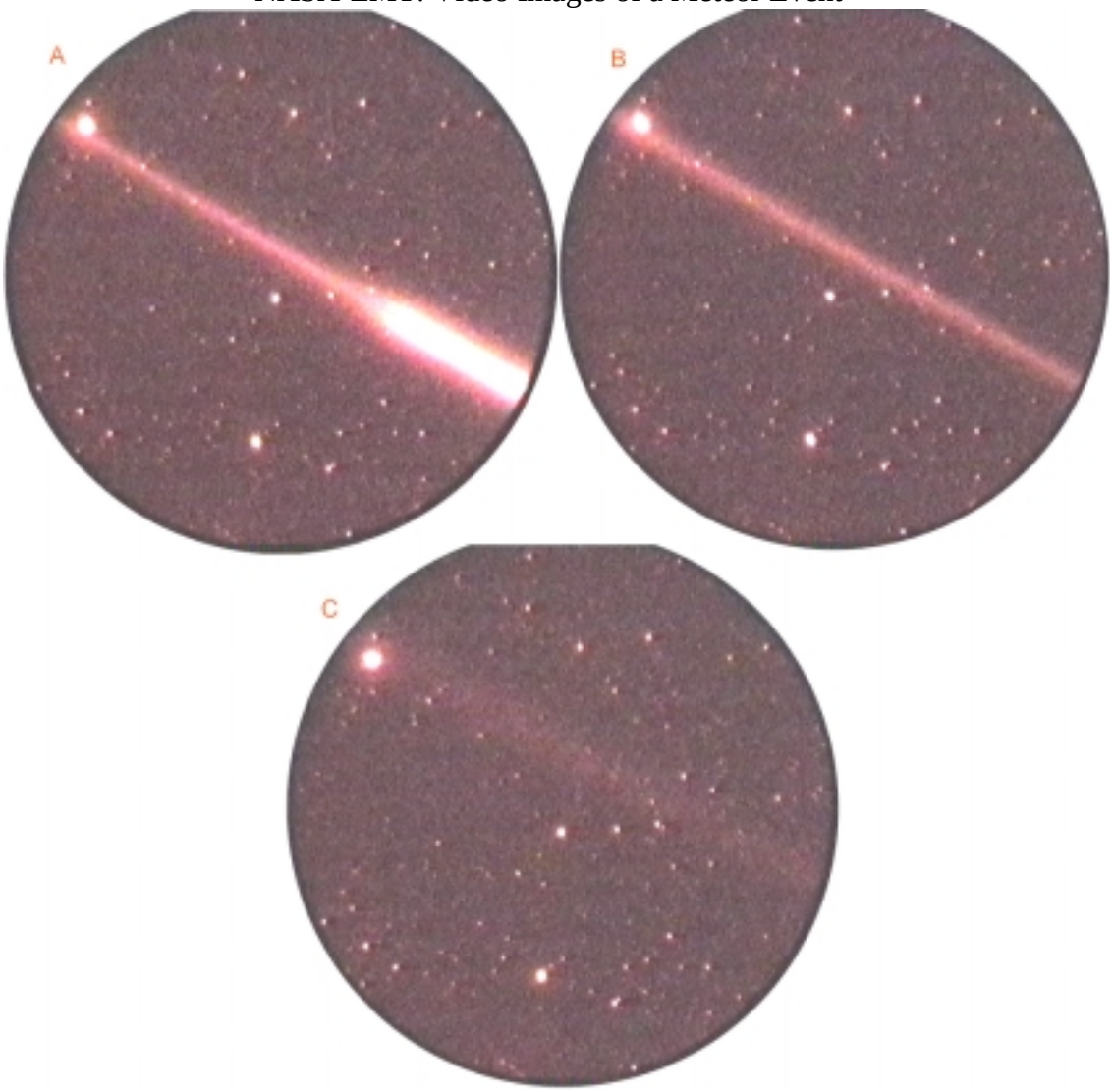

Figure IV.A-10. Time series of white light video images acquired with the NASA-LMT using the 40mm 2nd generation Micro-Channel Plate (MCP) intensified digital video camera. The field of view is 0.444 degrees in diameter. The interval between the first and seconds frames is 0.033 seconds. The interval between the second and third frames is tens times longer at 0.333 seconds. This is a meteor event clearly distinguished by the high angular velocity of the object and the residual plasma contrail. Meteor events must be separated from orbital object events to yield an accurate appraisal of the orbital population. Bright meteor events are easily distinguished by their residual contrail. Fainter meteors are identified by their appearance below the allowable earth shadow height, or at angular rate implying unbound orbits or altitudes well within the earth's atmosphere (~<200 km). Slower meteors which cannot be distinguished from faster orbital objects remain as a contaminant to the orbital object data set. The limiting apparent magnitude with this detector is approximately 16.5.

orbital object events and a meteor event as acquired with the LSP 2K CCD in both DM and sidereal drift-scan mode and with one of the 40mm MCP intensified video cameras.

The results from 400 of the approximately 750 hours of orbital object MCP intensified video data collected thus far by the NASA-LMT at NODO were published by Africano et al. (1999). The processed data were acquired from October 1997 through January 1999 using the 40 mm MCP intensified video camera described in Chapter IV. The consolidated annual pattern of these observations is shown in Figure VI.A-11. The butterfly shape arises from the restriction of orbital object observations to conditions near astronomical twilight (12 to 18 degree solar depression angle) where the LEO debris of primary interest to NASA is solar illuminated (~500 km). For summertime in the northern latitudes, these favorable conditions persist throughout most of the night, hence the widening trace near mid-year (Day of Year (DOY) =180). The horizontal gaps in the dataset occur during full moon and conditions of poor weather in the winter months, or a combination of poor weather and high insect population in the summer months. To maximize efficiency, vertical gaps are utilized for astronomical observations - in this way orbital object and astronomical data can be acquired without conflict.

The altitude and inclination distribution of these data at various altitude scales are shown in Figures VI.A-12 through 14. The vertical inclination groupings correlate with known rocket body breakups (Johnson et al. 1998). The grouping near 100 degree orbital inclination resulted from disruptions of the second stage boosters of Delta rockets employed to place the Landsat series and certain weather satellites into sun synchronous orbits. These orbits precess at a rate that maintains a constant solar phase angle between

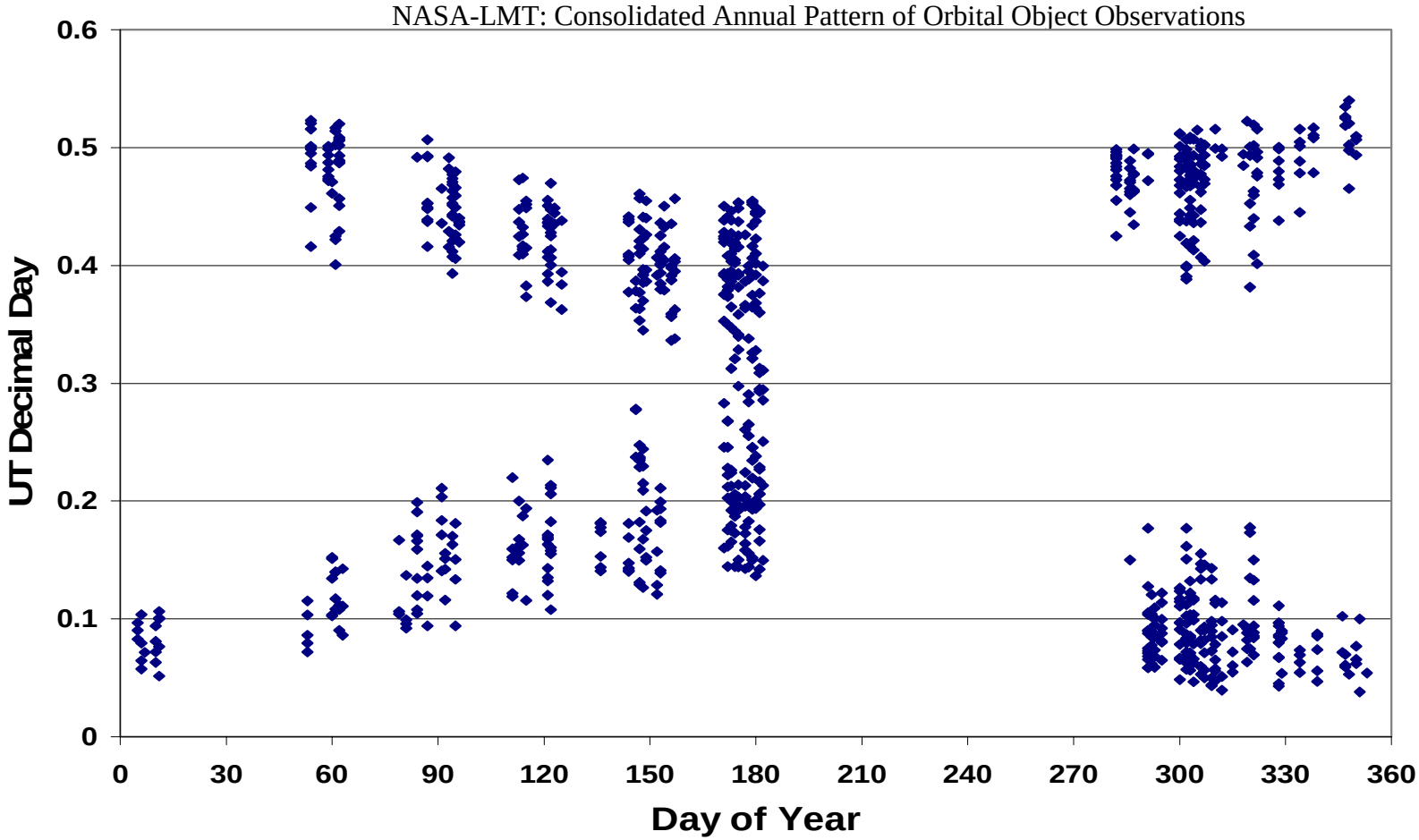

Figure VI.A-11. The consolidated annual pattern of orbital object observations for the NASA-LMT. The characteristic butterfly shape arises from the concentration of observations at low solar depression angles near astronomical twilight (12 to 18 degree solar depression) where the earth's shadow is sufficiently low to illuminate LEO debris at less than 2000 km altitude. Horizontal gaps arise during full moon and seasonal cessation of operations due to inclement weather and/or annual moth infestations. Data are for Oct 1997 through Jan 1999. (Africano et al. 1999)

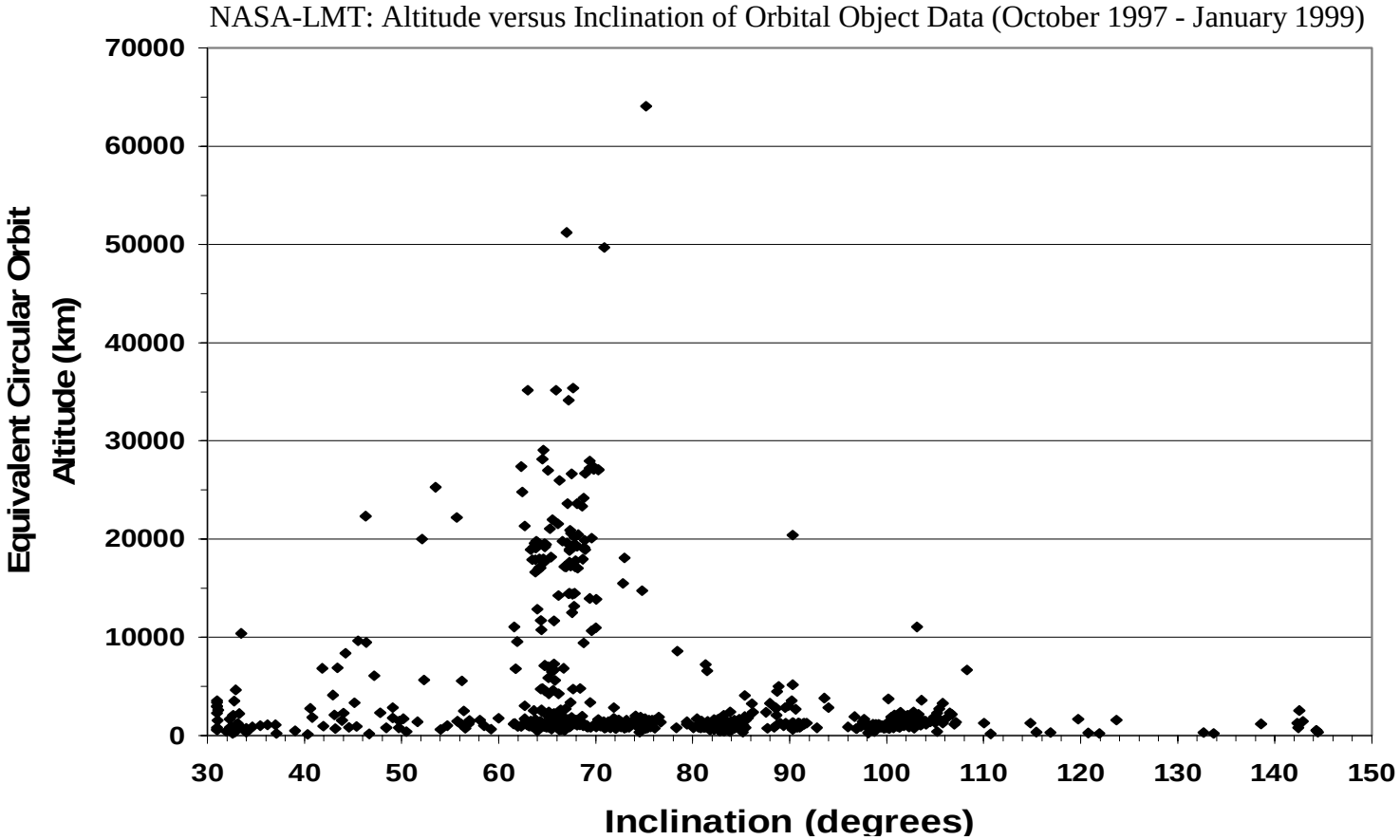

Figure VI.A-12. An altitude versus inclination plot derived from 400 of the approximately 750 hours of orbital object data acquired with the NASA-LMT at NODO through July 2000. The altitude is determined from the measured object angular rates coupled with the assumption of a circular orbit. The inclination is determined by the position angle of object motion through the FOV. The bulk of the orbital population is at LEO altitudes as can be seen in the next two plots. The peak near 65 degree inclination results primarily from high-altitude high eccentricity Russian satellites. Plotted data are from October 1997 through January 1999 and excludes meteor events based on shadow height restrictions. (Africano et al. 1999)

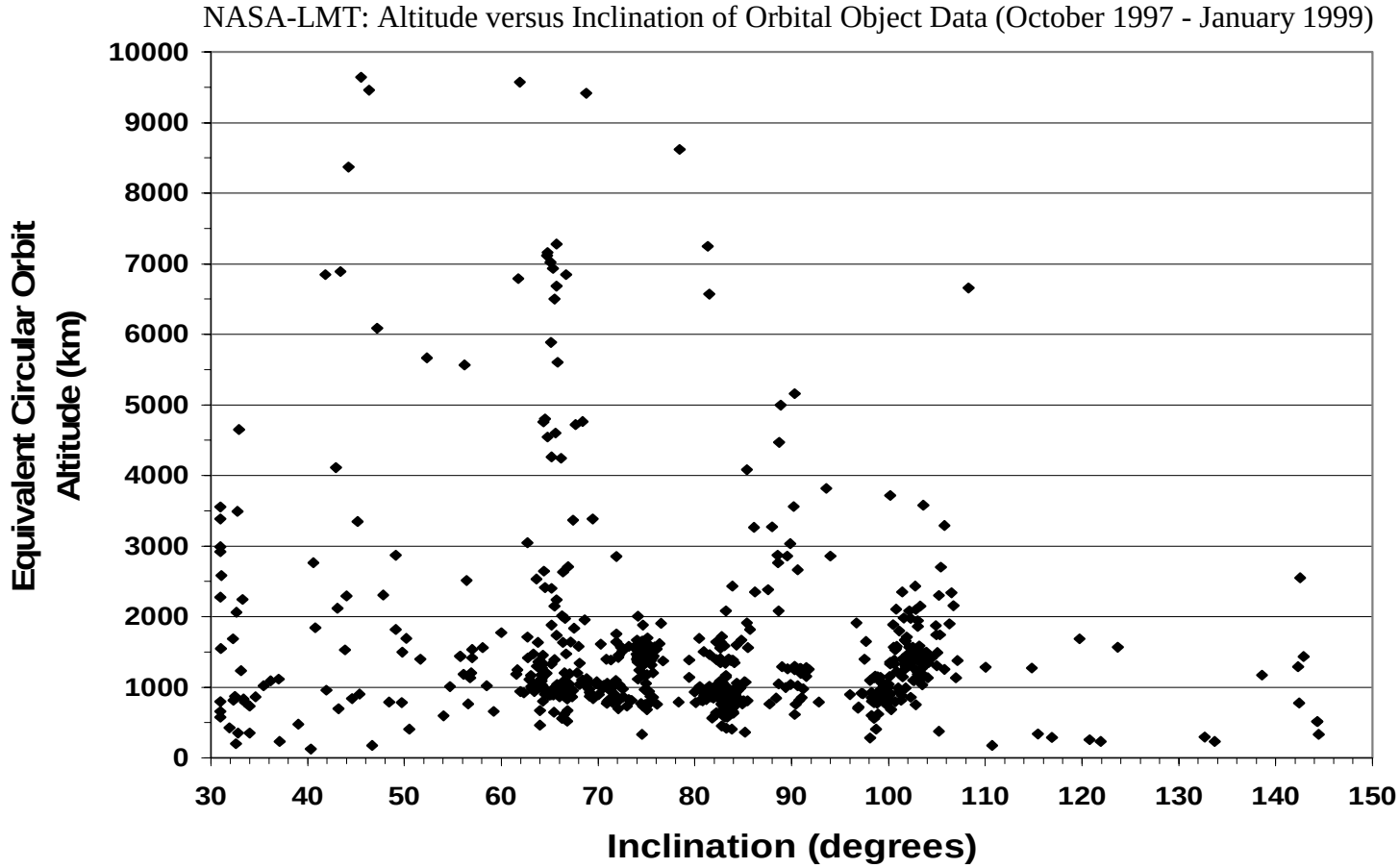

Figure VI.A-13. An altitude versus inclination plot identical to Figure VI.A-12 except scaled to display altitudes below 10,000 km. The distinct vertically oriented inclination clusters are due primarily to orbital debris objects from resulting from fragmentations of rocket bodies and satellites launched from Baikonour, Russia (65 to 75 degrees) and sun-synchronous satellites (95 to 105 degrees) launched by the United States. Plotted data are from October 1997 through January 1999 and excludes meteor events based on shadow height restrictions.(Africano et al. 1999)

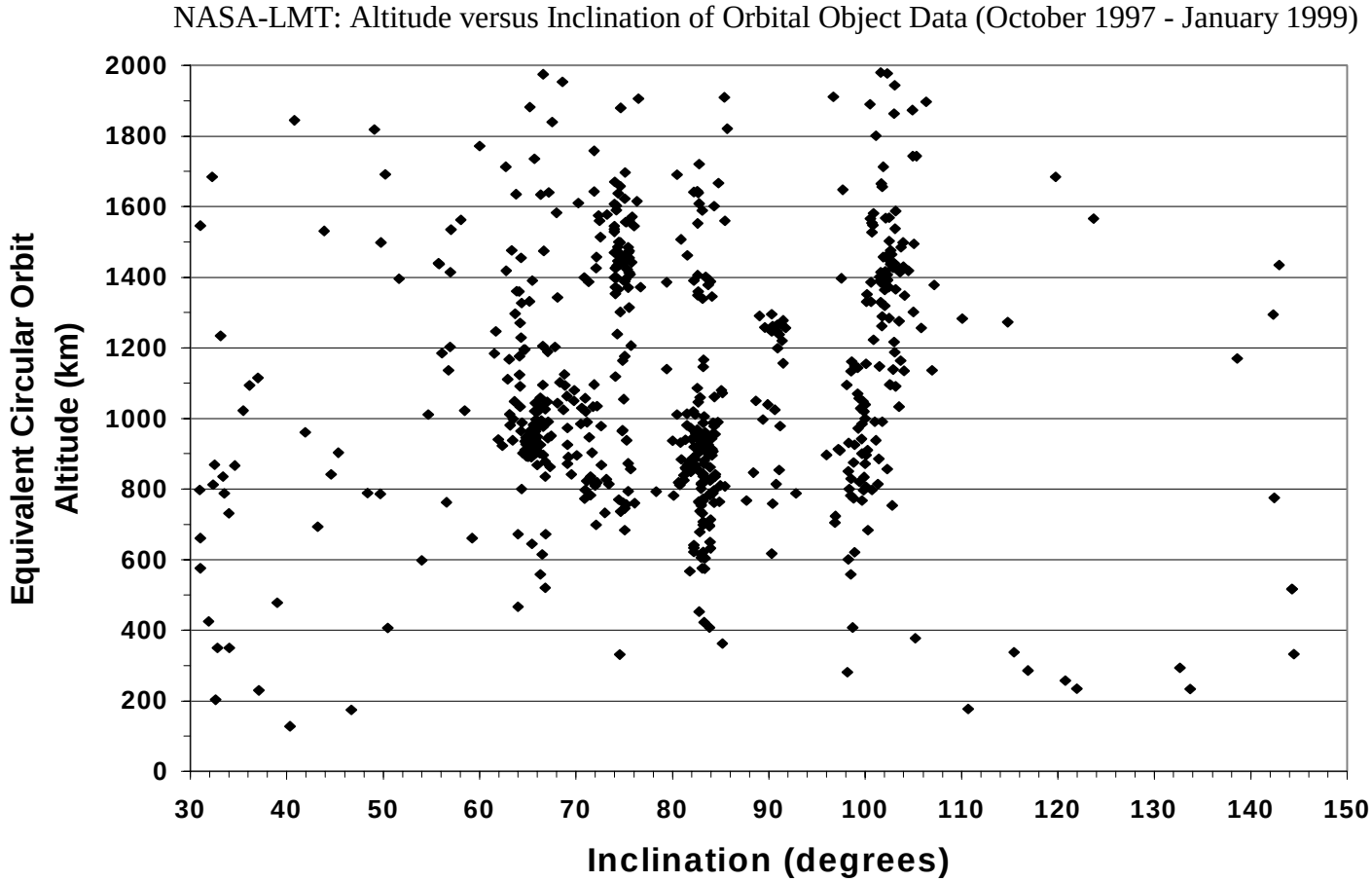

Figure VI.A-14. An altitude versus inclination plot identical to Figures VI.A-12 and 13, except scaled to display altitudes below 2,000 km. The distinct vertically oriented inclination clusters are due primarily to orbital debris objects from resulting from known fragmentations of rocket bodies and satellites. Events with circular orbit derived altitudes of less than 400 km are primarily meteors, but cannot be eliminated based on shadow height restrictions. Plotted data are from October 1997 through January 1999 and excludes meteor events based on shadow height restrictions. (Africano et al. 1999)

between the satellite and the sun for the sub-satellite point on the earth, thus enabling imaging at constant light and shadow conditions over the earth's surface. The disruptions of the Delta boosters occurred as much as 20 years after payload deployment when their hypergolic fuels mixed after corrosive fuel tank failures. Unspent rocket fuels are now routinely consumed or expelled from contemporary vehicles to mitigate this hazard. Another prominent grouping near 65 and 75 degree inclination resulted from the breakup of a series of rocket bodies and payloads launched notheastward by the former Soviet Union from their Baikonour site at 45.5 N degree latitude. Other prominent breakups, including the disruption of satellites and rocket bodies launched into low-inclination orbits by the European Space Agency (ESA) from their Kourou, French Guiana site at 5.23 degree latitude, are not visible to the NASA-LMT from NODO which, because it is zenith staring, can only observe orbital inclinations greater than or equal to its 33 degree latitude.

The aforementioned figures have had meteor events removed in accordance with shadow height restrictions. Objects with angular rates indicating elliptical orbit perigee altitudes below the earth's shadow height at the time of the observations are presumed to be meteor events. Those meteors with slower angular rates, placing them above the earth's shadow height, cannot be excluded unless their paths clearly begin or terminate with the FOV, or they leave a prominent contrail. Figure VI.A-15 shows the NASA-LMT orbital object dataset along with the shadow height curves delineating definite meteor events.

For the orbital object observations which correlated with the SATCAT catalogue,

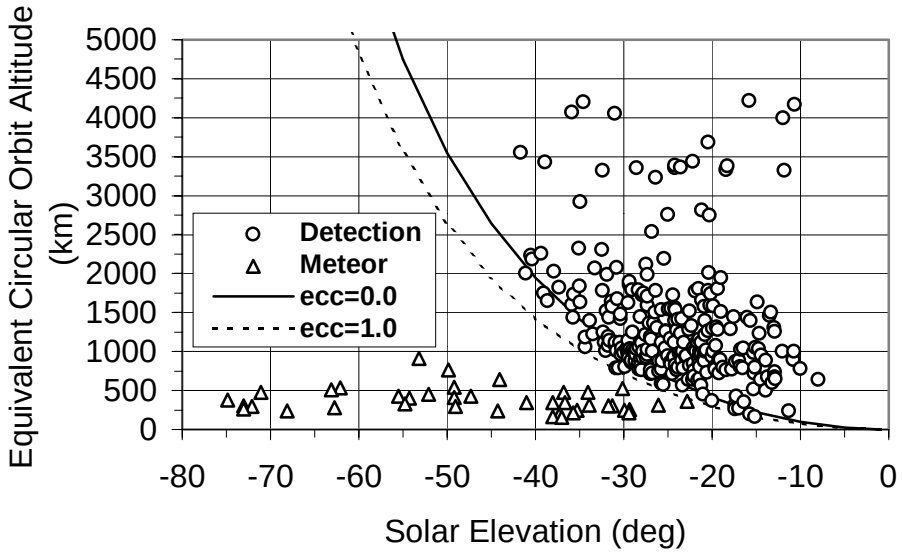

Figure VI.A-15. A demonstration of the delineation of meteor events based upon earth's shadow height restrictions. All NASA-LMT detections below 4500 km are plotted as a function of solar depression angle as derived from the time and date of the observations. The two curves show the circular orbit height and the elliptical orbit height (with eccentricity of 1.0 and assuming observations at perigee) expected of an orbiting object. Events below the latter curve must be meteor events (indicated by triangles). Meteor events in the region above the shadow height curve cannot be differentiated unless they leave a contrail of clearly begin or end within the FOV. (Africano et al 1999).

and thus had an independent measure of diameter, Figure VI.A-16 shows a plot of the absolute magnitude of each event versus the RADAR cross-section (RCS) derived diameter. These data have confirmed the mean albedo results of Henize et al (1993), with a 0.1 albedo fitting the center of the distribution. The absolute magnitude (M_{ABS}) in this connection is simply the observed apparent magnitude (M_{ABS}) of each event normalized to a 1000 km distance:

$$M_{ABS} = M_{APP} - 5 \cdot \log\left[\frac{Altitude(km)}{1000}\right] \qquad \text{(VI.A.a)}$$

Using the absolute magnitude and 0.1 mean albedo estimate, the number distribution as a function of object size is shown in Figure VI.A-17. This plot shows both catalogued (SATCAT) and un-catalogued objects (uncorrelated targets, UCTs). It clearly demonstrates a 1 cm limiting detection diameter for the NASA-LMT when equipped with the 40mm MCP intensified video camera. The figure also illustrates, via the large number of fainter UCTs, the incompleteness of the primarily RADAR-based SATCAT at small sizes. The SATCAT completeness falls rapidly relative to the NASA-LMT observations for diameters smaller than approximately 15 cm. Figure VI.A-18 shows the NASA-LMT detection rate for all orbital objects (upper plot) and then compares the results in terms of flux above a 10 cm diameter with the results (lower plot) from the Haystack Long Range Imaging RADAR (LRIR; Chapter II). The close agreement demonstrates the LMTs complimentary role with the RADAR in the acquisition of orbital object data.

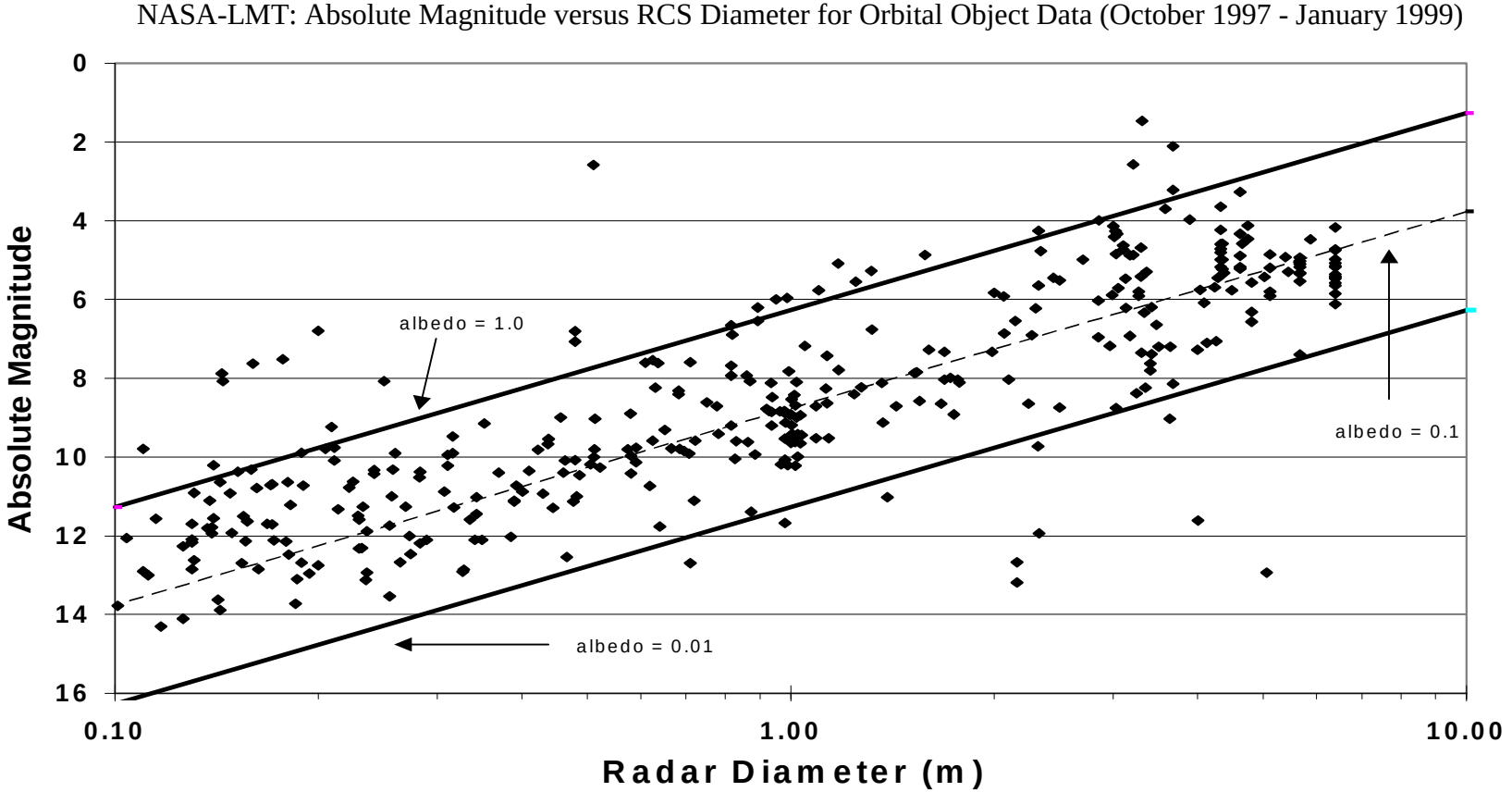

Figure VI.A-16. An absolute magnitude versus RADAR cross-section derived (RCS) diameter plot derived from 400 of the approximately 750 hours of orbital object data acquired with the NASA-LMT at NODO through July 2000. The absolute magnitude is simply the apparent magnitude normalized to a circular orbit altitude of 1000 km. The center of the distribution is fit by a 0.1 albedo, although individual objects vary significantly in reflectivity. Data points beyond 1.0 albedo may be due to specular reflections or an RCS-based diameter smaller than the object actual physical size. Plotted data are from October 1997 through January 1999 and excludes meteor events based on shadow height restrictions. (Africano et al. 1999)

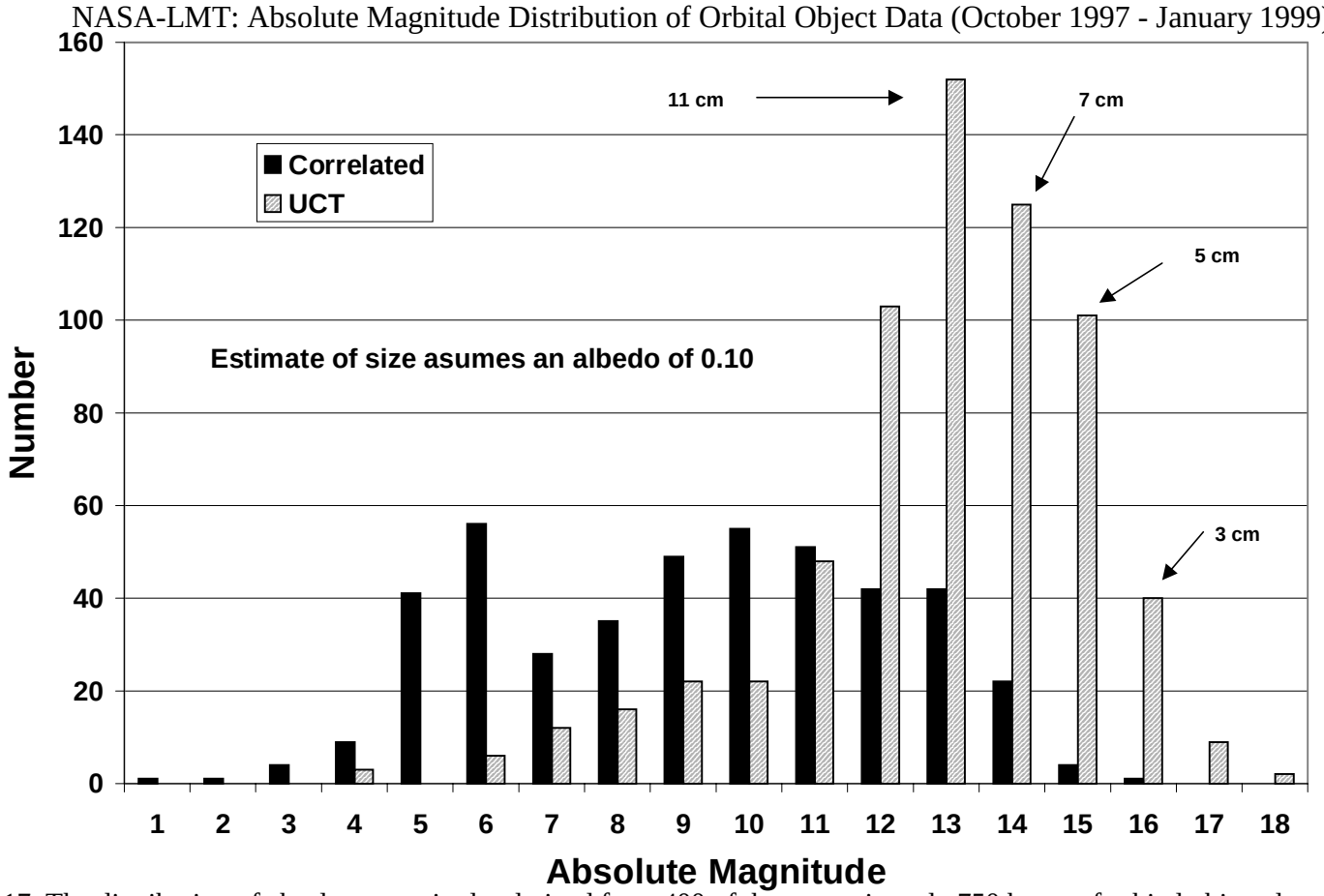

Figure VI.A-17. The distribution of absolute magnitudes derived from 400 of the approximately 750 hours of orbital object data acquired with the NASA-LMT at NODO through July 2000. The NASA-LMT is detecting objects significantly fainter than those in the SATRAK catalogue. The limiting diameter based upon a 0.1 albedo is approximately 1 cm. Horizontal errors are approximately +- 0.75 magnitude, vertical errors are ~ +- 15 counts. Plotted data are for October 1997 through January 1999 and exclude meteors based on shadow height restrictions.(Africano et al. 1999)

NASA-LMT: Orbital Object Detection Rate and Flux (October 1997 - January 1999)

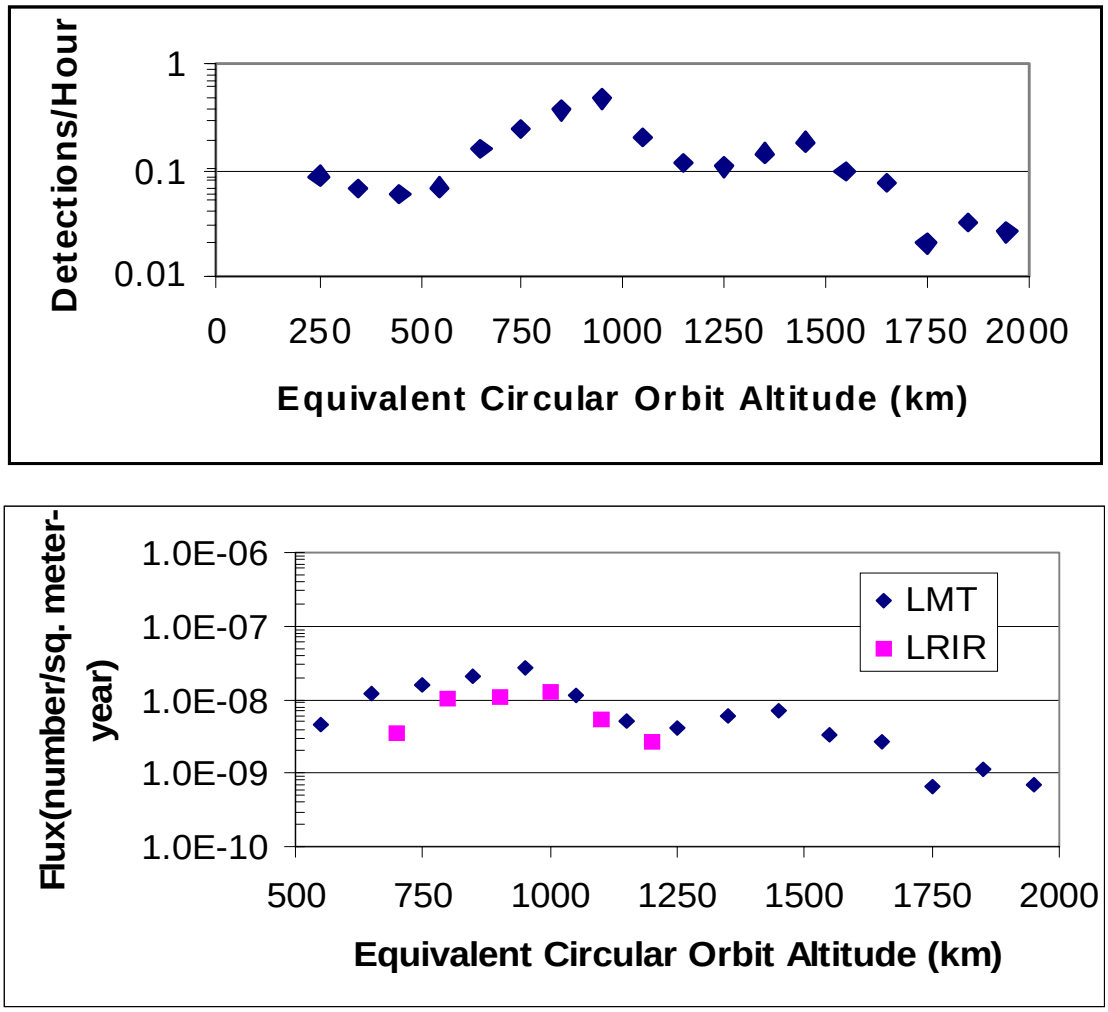

Figure VI.A-18. The object detection rate (upper plot) and the orbital object flux (lower plot) as a function of circular orbit altitude. The detection rate figure is for all sizes whereas the flux plot is only for diameters greater than 10 cm. The NASA-LMT data agree with results from the Haystack Long Range Imaging RADAR, indicating that they view a substantively similar population. Plotted data are from October 1997 through January 1999 and excludes meteor events based on shadow height restrictions. (Africano et al. 1999)

B. Astronomical Observations

The NASA-LMT has been involved in a multi-narrowband astronomical survey since the spring of 1996. As described in Hickson and Mulrooney (1998a), the purpose of the survey is to obtain object classifications, spectral energy distributions, and multi-narrow band photometric redshifts for all galaxies and quasars (QSOs) to a limiting z of approximately 0.5 in a 20 square degree strip of sky ranging from 12 to 18 hours Right Ascension (R.A.) and centered on the 32.979 N degree Declination (Dec) accessible to the NASA-LMT at zenith. As shown in Figure VI.B-1, the strip is at high galactic latitude and passes within 7 degrees of the north galactic pole (NGP). These data will be used to study galaxy and QSO evolution and morphology as well as the large-scale structure of the universe. A two-dimensional R.A. wedge analogous to the “straw person” diagram (Appendix D) of de Lapparent et al (1986), but with a 15-fold increase in coverage depth, will be generated for the NODO survey strip. Sheets, shells, or filamentary structures should be readily evident. The photometric accuracy of the multi-narrow band survey, yielding $\Delta z \leq 0.02$, is equivalent to what could be obtained spectroscopically (Hickson, Lanzetta PC) and should have sufficient distance resolution to enable the differentiation between cosmic string and cold dark matter (CDM) models based upon the topology of the galaxy distribution. Even galaxy morphologies may be differentiated via multi-narrowband photometry (Hickson PC). With the difficulties involved in obtaining large blocks of observing time on conventional telescopes, having the NASA-LMT as a large dedicated survey instrument has been crucial to obtaining a data set with sufficient depth

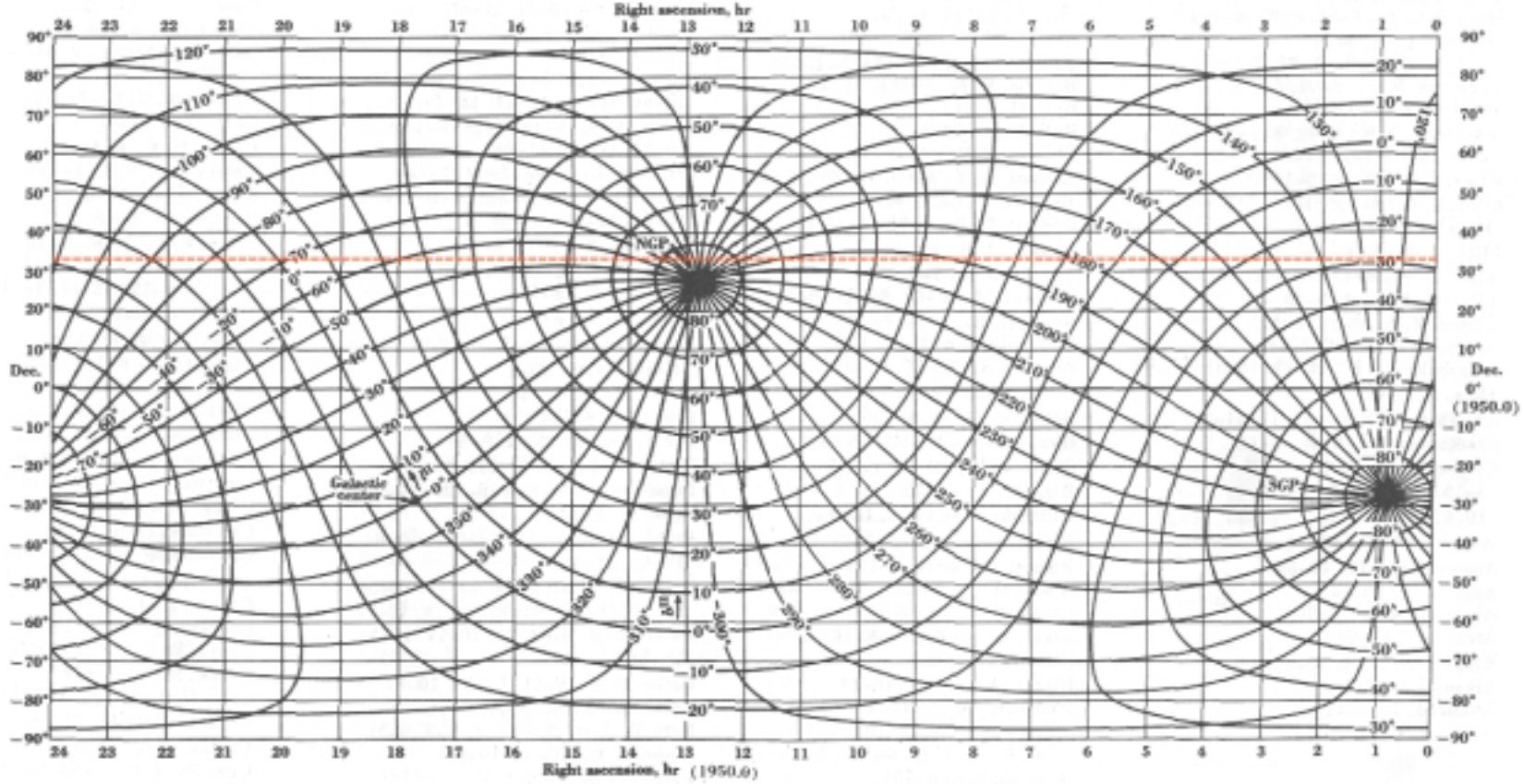

Figure VI.B-1. A plot mapping astronomical Right Ascension (R.A.) and Declination (Dec) relative to Galactic Latitude and Longitude. Extragalactic astronomical survey data is acquired primarily at galactic latitudes greater than 25 degrees from the galactic plane in order to reduce field crowding from stars which might otherwise contaminate photometric measurement of galaxies and QSOs. The red line corresponds to NODO's latitude (32.979408 N degrees) which, since the LMT is a zenith staring instrument, is also the central declination of the survey strip. The primary observing season is springtime where the high galactic latitude R.A. range is 8 to 18 hrs. A high galactic latitude R.A. range of only 4 hrs (22.5 to 2.5 hrs) is available in the fall season. (Credit: Kraus 1986).

and field coverage to perform this broad survey.

The first phase of the survey was recently completed in May 2000 and consists of data acquired using both the LSP 2K and PV 1K CCDs. The second phase will begin in March 2001 using the new PV 2K CCD, doubling both the survey area and the effective exposure time. Thus far, approximately 135 nights of data have been collected through 35 narrow band (10 nm wide) interference filters with center wavelengths ranging from 454.5 to 989.7 nm, and through four broadband (BVRI) filters. Transmission curves for the each broadband filter and the narrowband set are shown in Appendix E. Preliminary object counts and a magnitude distribution for a subset of the data are shown in Figures VI.B-2 and 3. Hickson, using his LMTPHOT software package, has performed the astrometry and photometry of the complete 100+ GB data set and expects to have the preliminary analysis ready for publication by the close of 2000.

The survey data have been calibrated using a set of tertiary spectrophotometric standard stars which were obtained via observations at Kitt Peak National Observatory (KPNO) in 1997 (Hickson and Mulrooney 1998b). The standards are conveniently spaced at 30 minute R.A. intervals within the survey strip so that drift-scanned data may be accurately calibrated under varying observing conditions throughout a night's observations. An R band image of one of the standard stars acquired with the NASA-LMT equipped with the drift-scanning PV 1K CCD is shown in Figures VI.B-4 and 5 along with a first generation Palomar Sky Survey (POSS) print acquired with the red sensitive (103aE) emulsion. The LMT and POSS exposure times are 78 and ~300 seconds respectively. Based upon this calibration standard star (red arrow) with an R

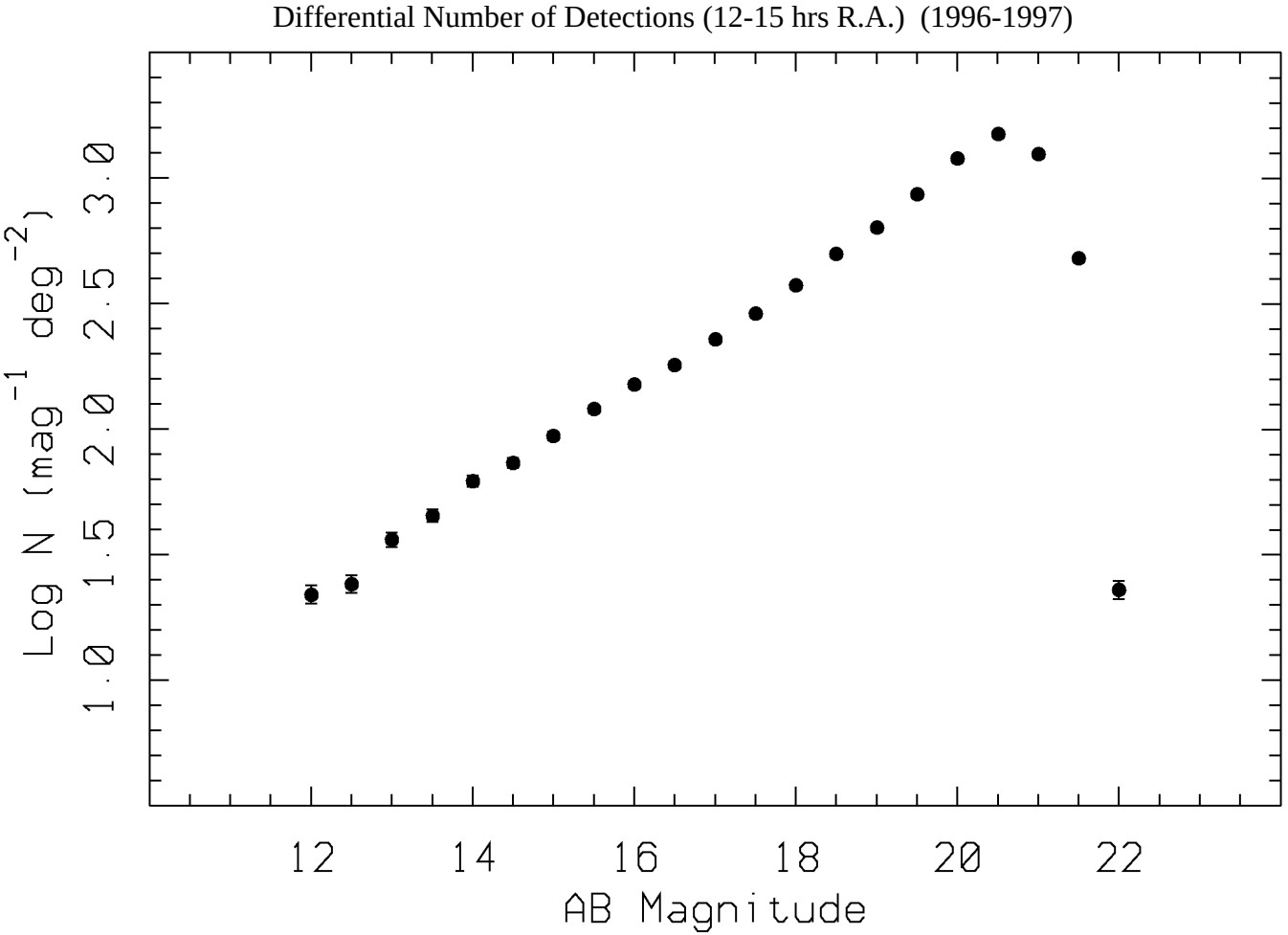

Figure VI.B-2. A plot showing differential detections as a function of AB magnitude as defined by Oke (1974) for a subset (12-15 hrs R.A.) of the astronomical survey data acquired during 1996 and 1997 with the LSP 2K CCD. The limiting magnitude for this set of survey data is approximately 21.5 as is evident from the sharp decline in object counts beginning at a magnitude of 20.5. (Credit: Hickson PC).

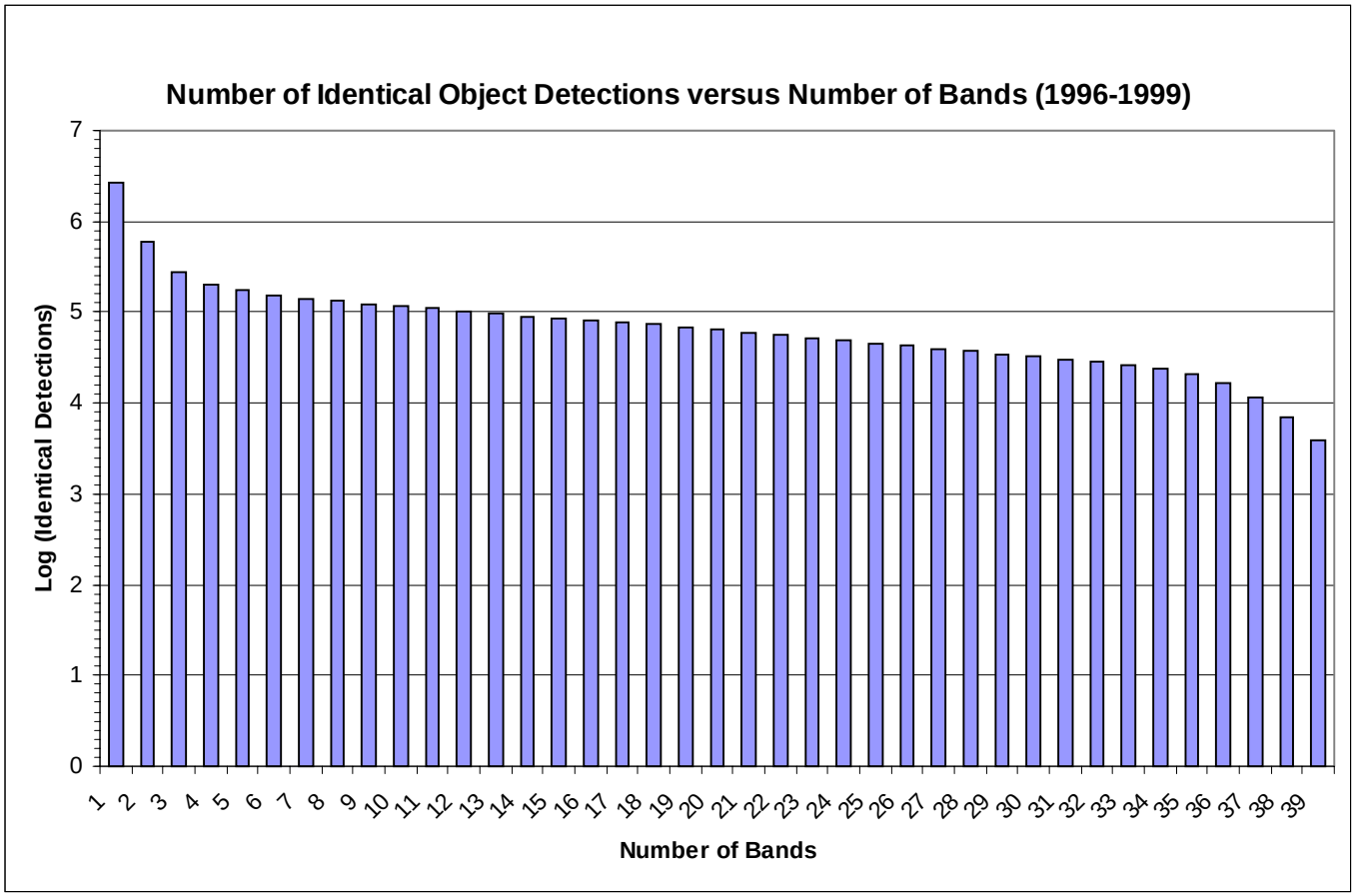

Figure VI.B-3. A plot showing the relationship between the number of identical astronomical object detections and the number of filters in which these identical objects appear. The data acquired in the spring of 2000 is not included. Only approximately 4000 objects were detected in all 35 narrowband and broadband (BVRI) filters, whereas approximately 2.5 million objects were detected in a single filter. Many of these latter detections are probably cosmic rays. Over 30,000 objects were detected in 30 filters, ~100,000 in 12 filters, and 59,238 objects were detected in the broadband BVRI filter set (data not shown).

NASA-LMT @ NODO: A Spectrophotometric Standard Star

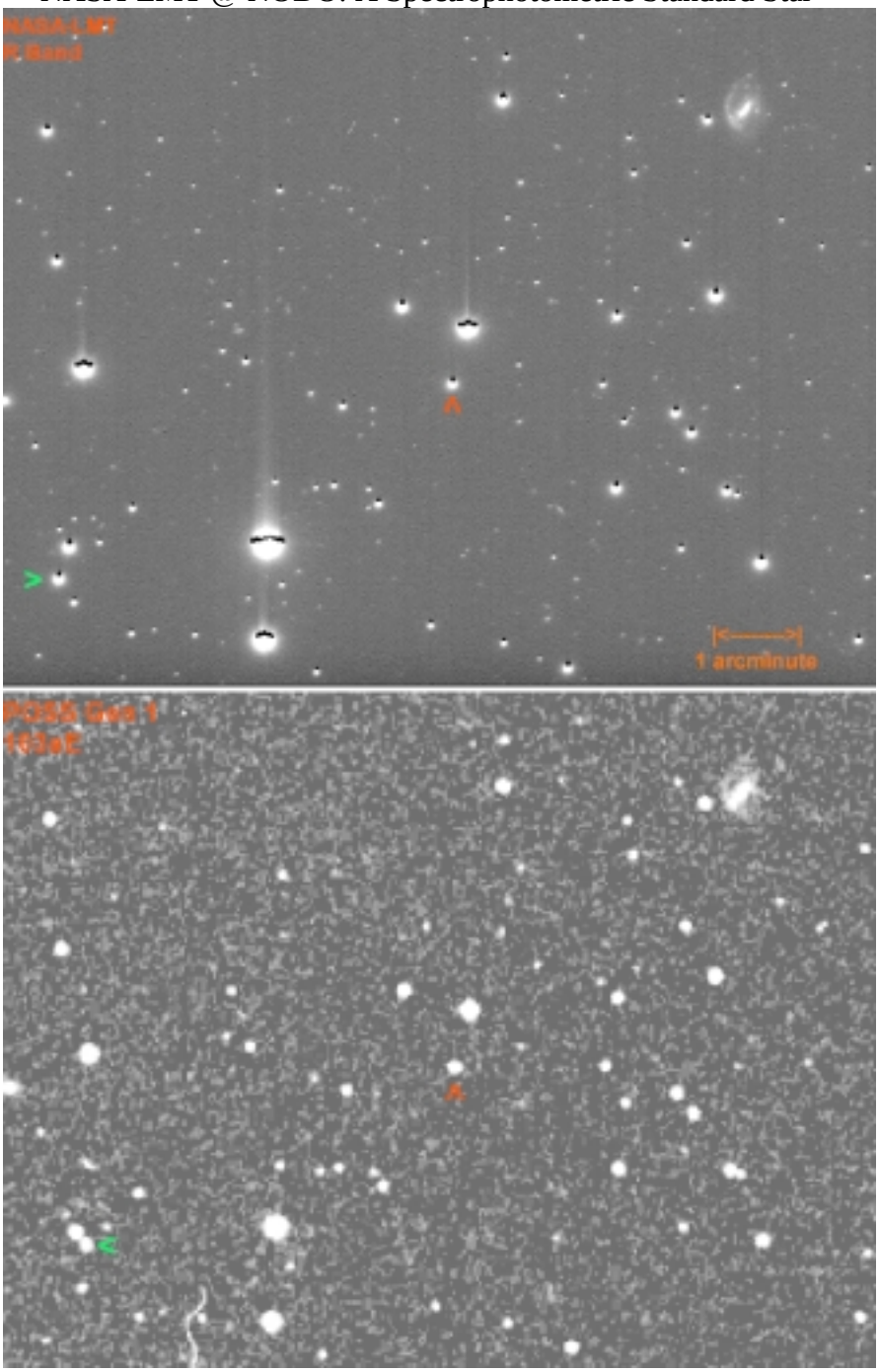

Figure VI.B-4. One of the calibration standard stars (1630+33, red arrow) in the NODO survey strip. The upper frame is an R Band NASA-LMT image acquired with the PV 1K CCD and the lower is a Palomar Sky Survey (POSS) digitized photographic print. Located at R.A.16.504 and Dec +32.903, the star has BVRI magnitudes of 16.44, 15.81, 15.63, and 15.41 respectively. The limiting magnitude in the upper R Band image at a SN ratio of 6.3 is 22.25. The difference in resolution and sensitivity between the two images is evident. The green arrow indicates a high proper motion star (~0.5 arcseconds/year) also shown in the next figure. North up, West at left.

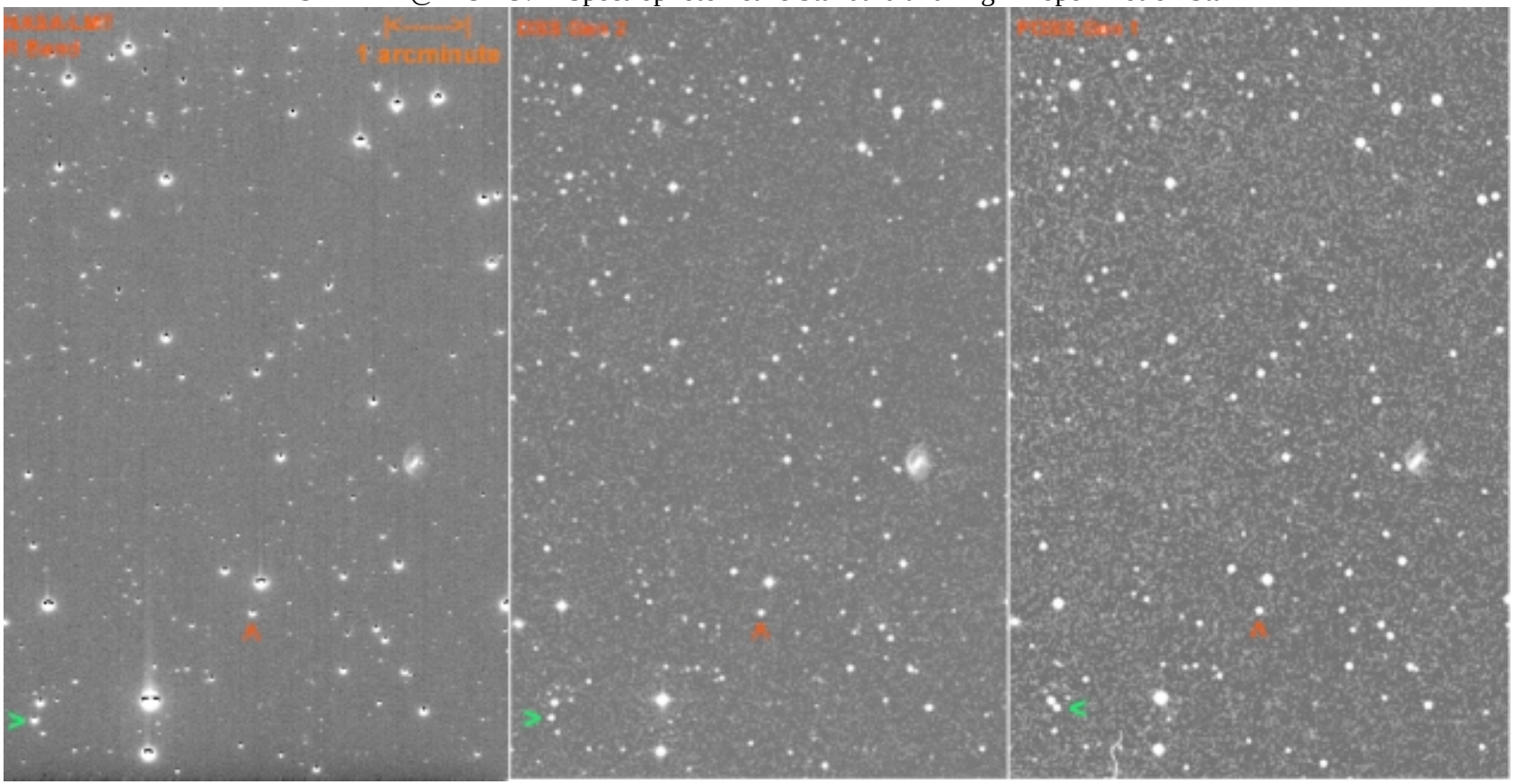

Figure VI.B-5. The field around the 1630+33 calibration standard star (red arrow) in Hercules. The three frames from left to right show an R Band NASA-LMT image acquired with the PV 1K CCD in May 2000, a 2nd generation Digital Sky Survey (DSS) red sensitive photographic image acquired April 1991, and a POSS red sensitive photographic image acquired in June 1954. Based on the calibration star, the limiting magnitude in the NASA-LMT R Band image at a SN ratio of 6.3 is 22.25. A star with a proper motion of 0.5 arcseconds/year is indicated by the green arrow. North up, West is at left.

magnitude of 15.63, the limiting detection magnitude for the displayed LMT field at a conservative SN ratio of 6.3 (2 magnitudes above background) is 22.25. Interestingly, a star with a proper motion of approximately 0.5 arcseconds/year is visible in the same field (green arrow). The second figure shows the same field areas along with a second generation Palomar Sky Survey R band image interposed. The three images were acquired in 1954, 1991, and 2000 respectively. The proper motion of the star (green arrow) is clearly evident, as is the enhanced resolution of the NASA-LMT image.

As a further demonstration of NASA-LMT optical performance, a series of sample images have been generated from the extensive survey data acquired to date. The majority of these images are color composites of broadband BVR data acquired in 1999 and 2000 with the PV 1K CCD. As a demonstration of the color separation process, Figure VI.B-7 shows separate B,V,R, and I band images acquired on different nights in 1999 and 2000 of the galaxy pair NGC 3424 and 3430. The B,V, and R images from this sequence have then been combined to produce the color composite shown in Figure VI.B-8. Other composites along with magnified insets showing both prominent and fainter galaxies are shown in Figures VI.B-9 through 20. Catalogue designations are indicated on the individual insets, but the vast majority of non-stellar objects visible in these images are un-catalogued (NC). The three best B, V and R nights were selected for each of these composites with resolution varying between 1.0 and 1.5 arcseconds. The individual B,V, and R limiting magnitudes for a 6.3 SN ratio, 4 pixel detection, are 22.82, 21.19 and 22.25 magnitudes respectively.

NASA-LMT: B,V,R, and I Broadband Images of NGC 3424 and 3430

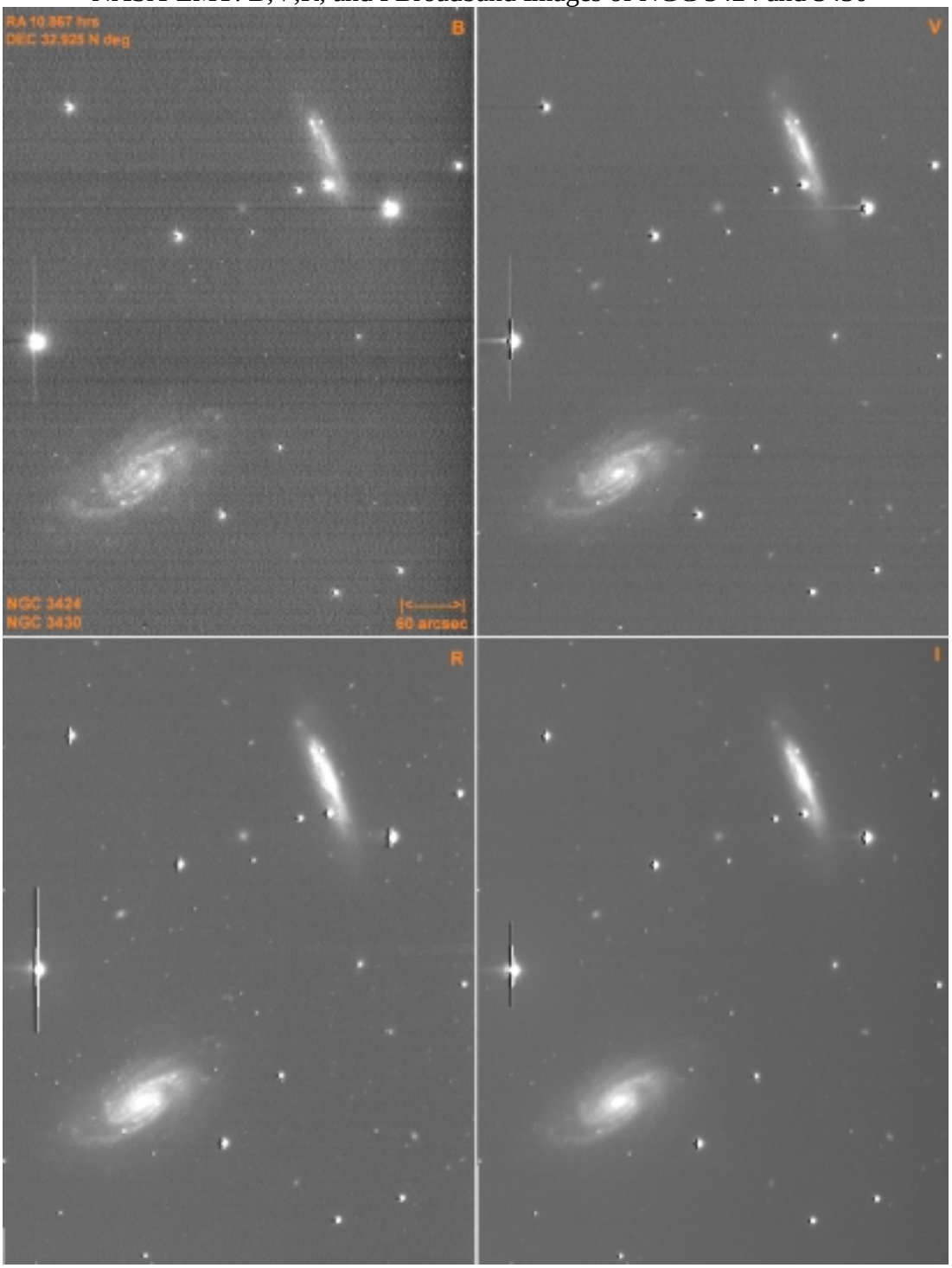

Figure VI.B-6. The galaxy pair NGC 3424 (upper) and 3430 (lower), in Leo Minor, as imaged with the NASA-LMT and PV 1K CCD through B,V,R, and I broadband filters in 1999 and 2000. The B,V, and R images were combined to generate the composite shown in the next figure. The galaxies have V magnitudes of 13.2 and 11.5 respectively. HII regions are clearly visible in the B Band image as bright knots in the spiral arms. West is up, North at left.

NASA-LMT: BVR Broadband Composite Image of NGC 3424 and 3430

Figure VI.B-7. A BVR Broadband composite of the galaxy pair NGC 3424 (upper) and 3430 (lower) in Leo Minor. The individual images were acquired with the NASA-LMT and PV 1K CCD through BVR filters in 1999 and 2000. The galaxies have V magnitudes of 13.2 and 11.5 respectively. The fainter galaxies are un-catalogued (NC). The limiting magnitude at a SN ratio of 6.3 is approximately 22.0. Perceived registration errors on brighter stars arise from the enhanced R and V sensitivity relative to B. Although not visible at this scale, residual corrector chromatic aberration does yield a small difference in the B,V, and R plate scales (<.004%). W is up, N left.

NASA-LMT: BVR Broadband Composite Image of NGC 3395 and 3396

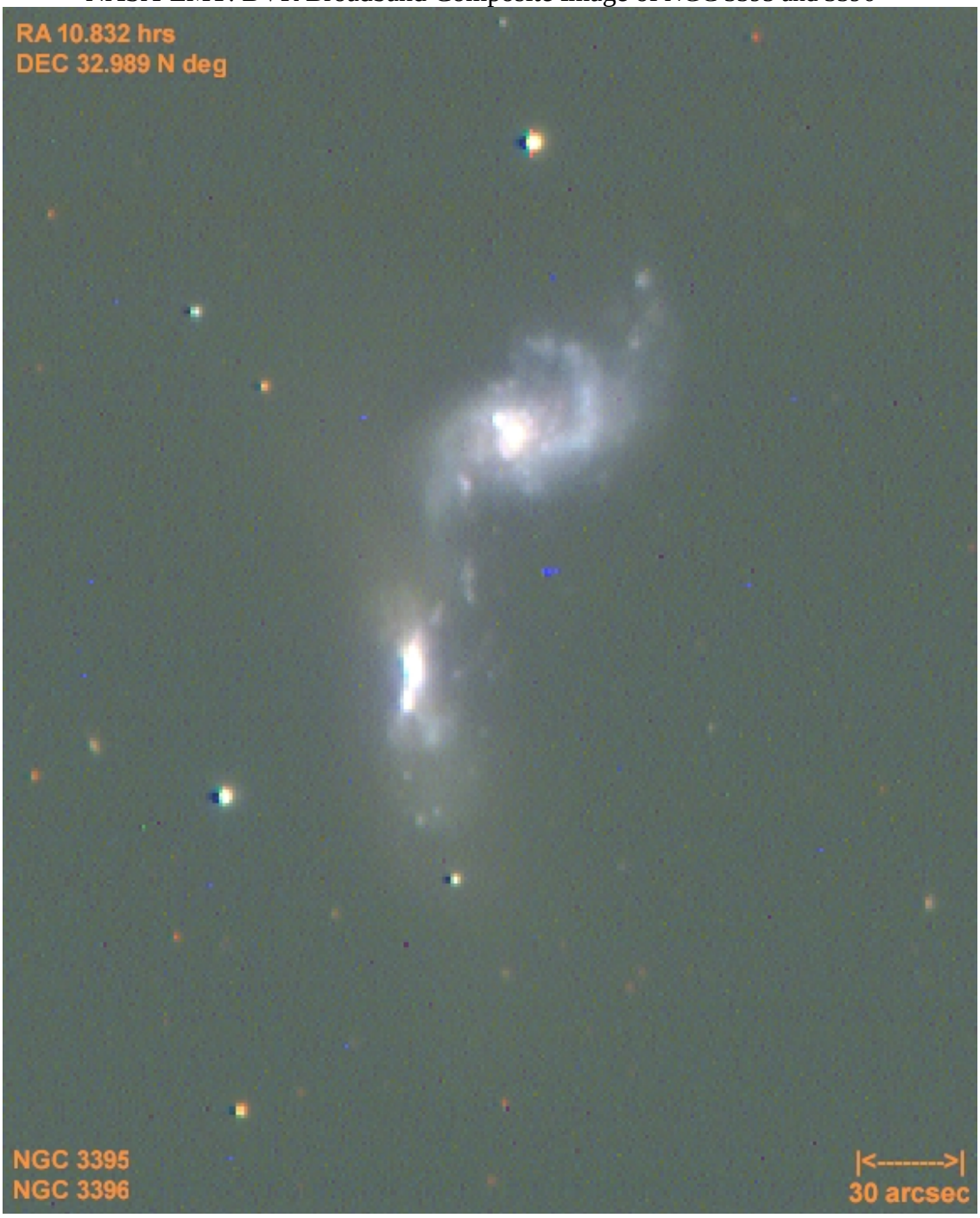

Figure VI.B-8. A BVR Broadband composite of the interacting galaxy pair NGC 3395 (upper) and 3396 (lower) in Leo Minor. The individual images were acquired with the NASA-LMT and PV 1K CCD through B,V, and R broadband filters in 1999 and 2000. The galaxies have V magnitudes of 12.0 and 12.6 respectively. The limiting magnitude for this frame at a SN ratio of 6.3 is approximately 22.0. West is up, North at left.

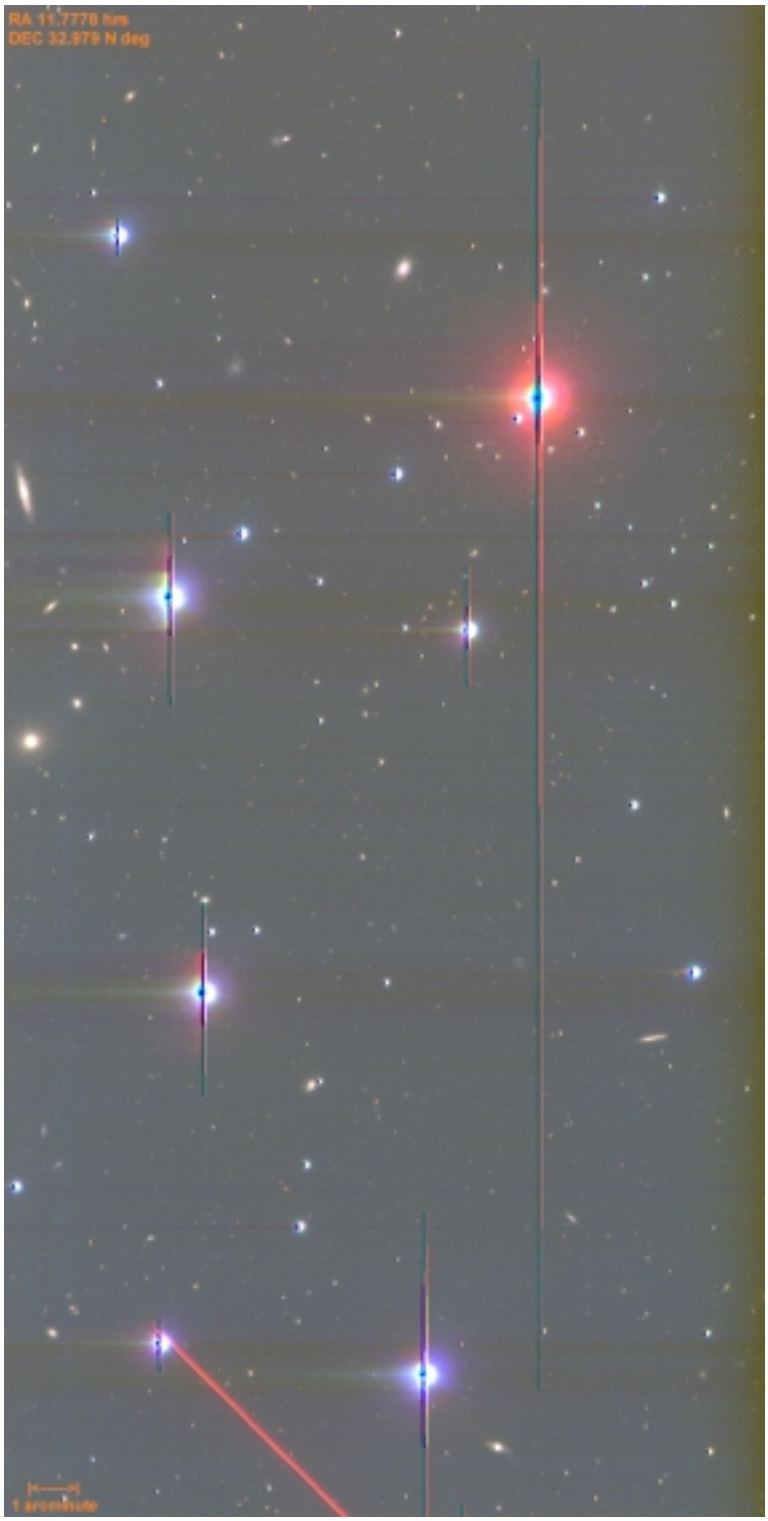

Figure VI.B-9. A BVR composite of a 30 arcminute long segment of the NASA-LMT survey strip in Ursa Major. The BVR images were acquired with the PV 1K CCD through broadband filters in 1999 and 2000. Sample galaxies from this frame are shown in the next figure. The red streak at bottom is a meteor or orbital object passing through the FOV while data was acquired with the R Band filter. Limiting magnitude at a 6.3 SN ratio is ~22.0. West up, North left.

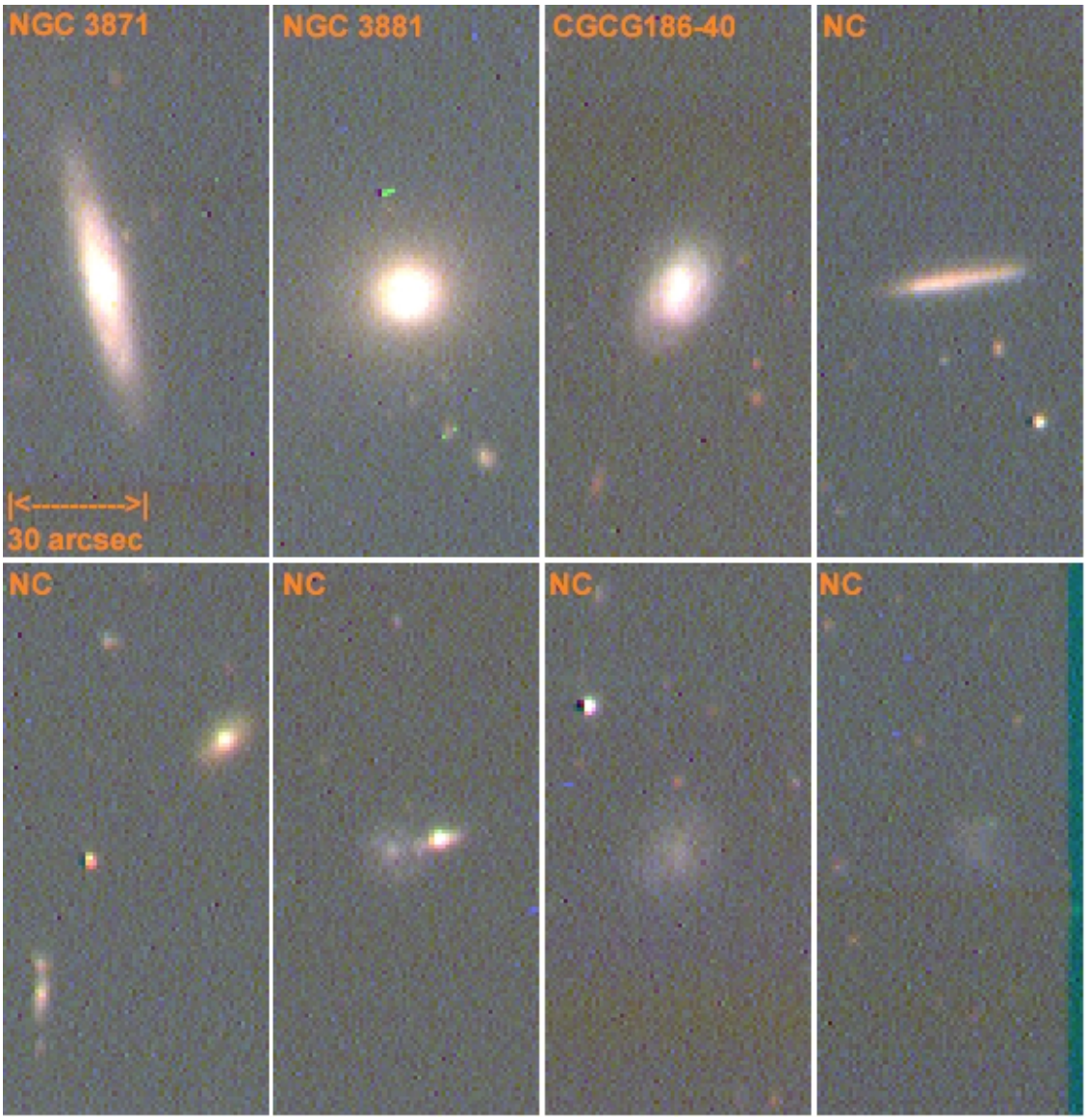

Figure VI.B-10. Sample galaxies in Ursa Major from the previous figure. From left to right, the three indicated catalogued galaxies have V magnitudes of 15.5, 15.3, and 15.6 respectively. Among the un-catalogued (NC) galaxies, the latter two are LSBs. Limiting magnitude at a 6.3 SN ratio is ~22.0. All frames are of identical scale. West is up, North at left.

Figure VI.B-11. A BVR composite of a 30 arcminute long segment of the NASA-LMT survey strip in Ursa Major. The BVR images were acquired with the NASA-LMT and PV 1K CCD through broadband filters in 1999 and 2000. Sample galaxies from this frame are shown in the next figure. Limiting magnitude at a 6.3 SN ratio is ~22.0. West is up, North at left.

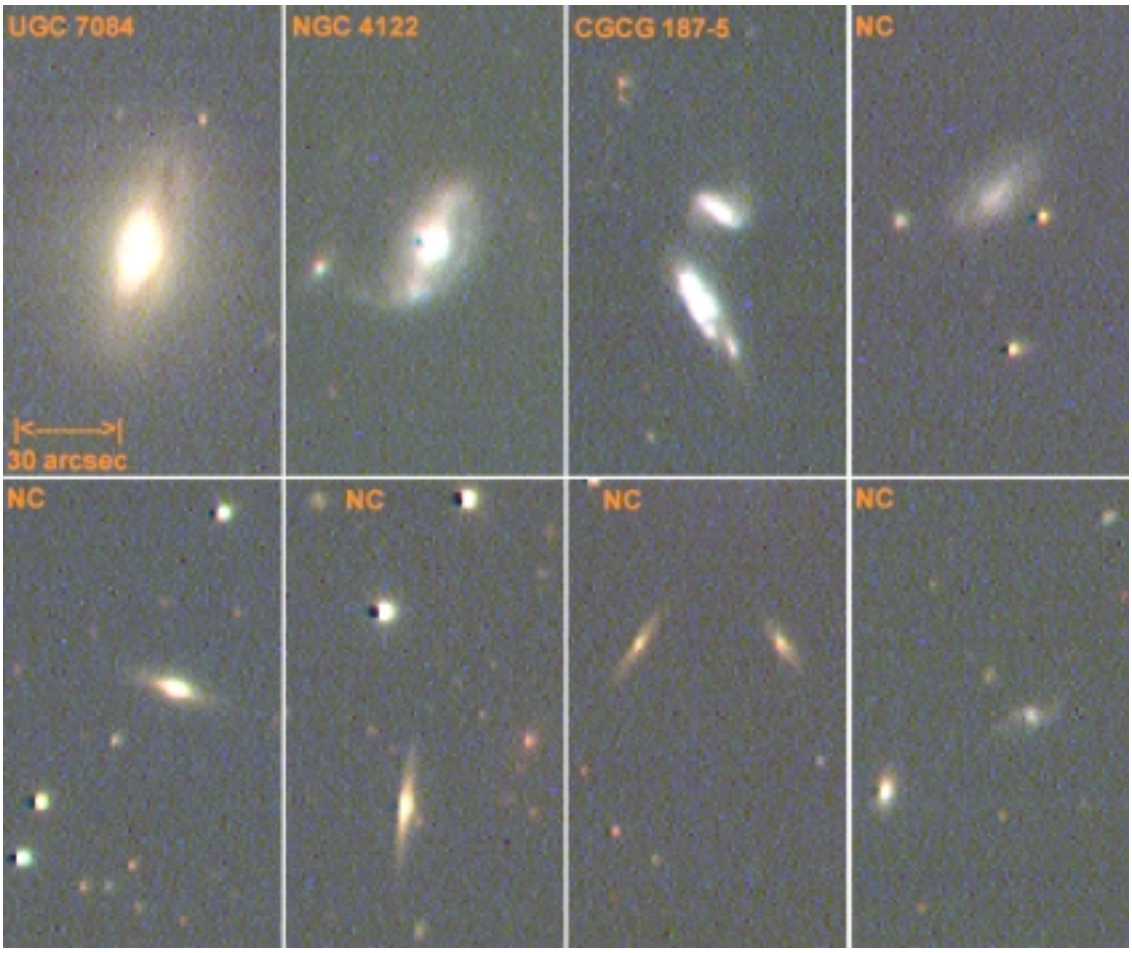

Figure VI.B-12. Sample galaxies in Ursa Major from the previous figure. From left to right, the three indicated catalogued galaxies have V magnitudes of 14.7, 14.9, and 17.2/16.5 respectively. The remainder are un-catalogued (NC) galaxies. Limiting magnitude at a 6.3 SN ratio is ~22.0. All frames are of identical scale. West is up, North at left.

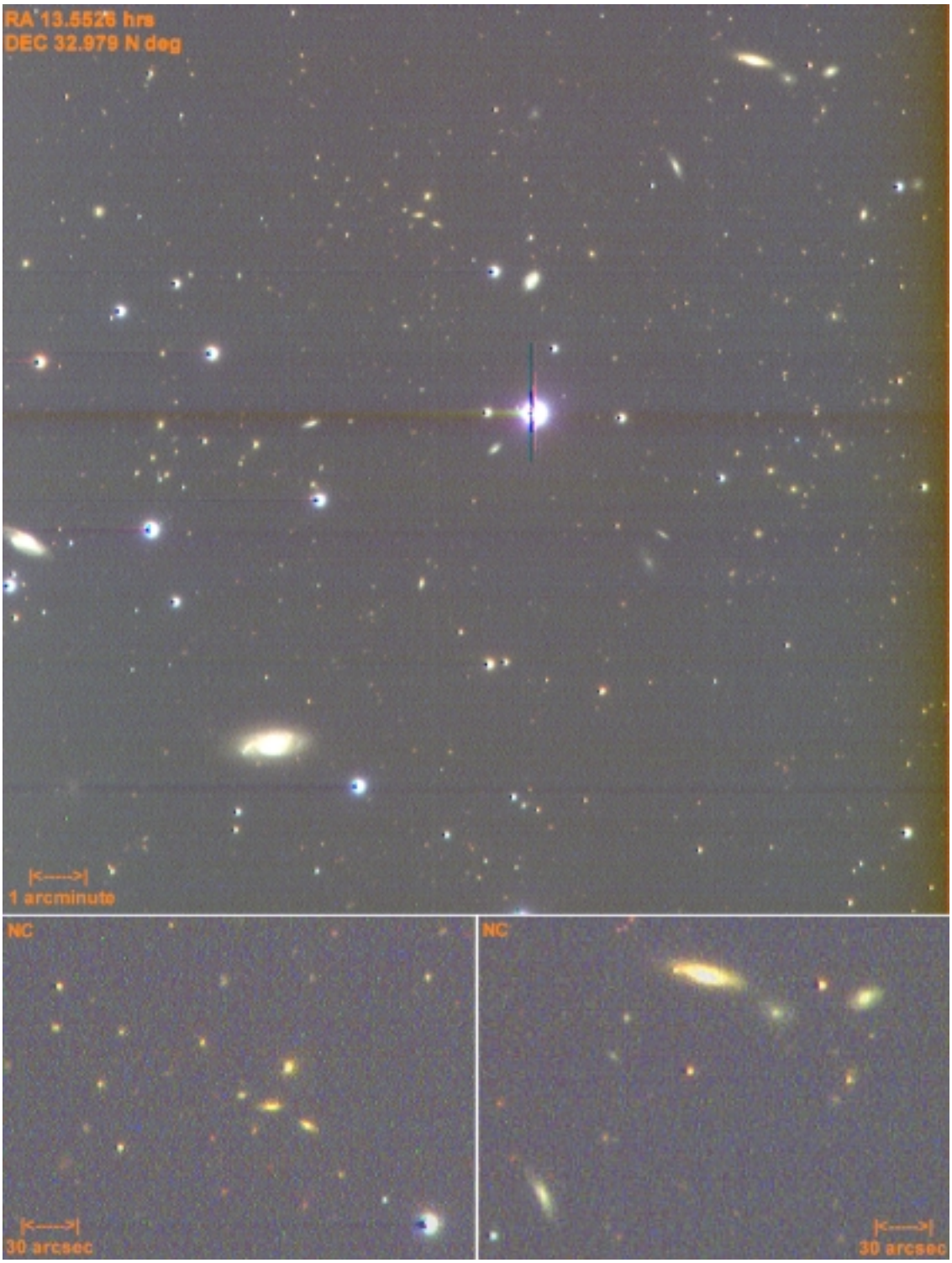

Figure VI.B-13. A BVR composite of a 16.48 by 15.5 arcminute segment of the NASA-LMT survey strip in Canes Venatici. The BVR images were acquired with the PV 1K CCD through broadband filters in 1999 and 2000. The insets show enlargements of field portions containing galaxy groups. Limiting magnitude at a 6.3 SN ratio is 22.0. West is up, North at left.

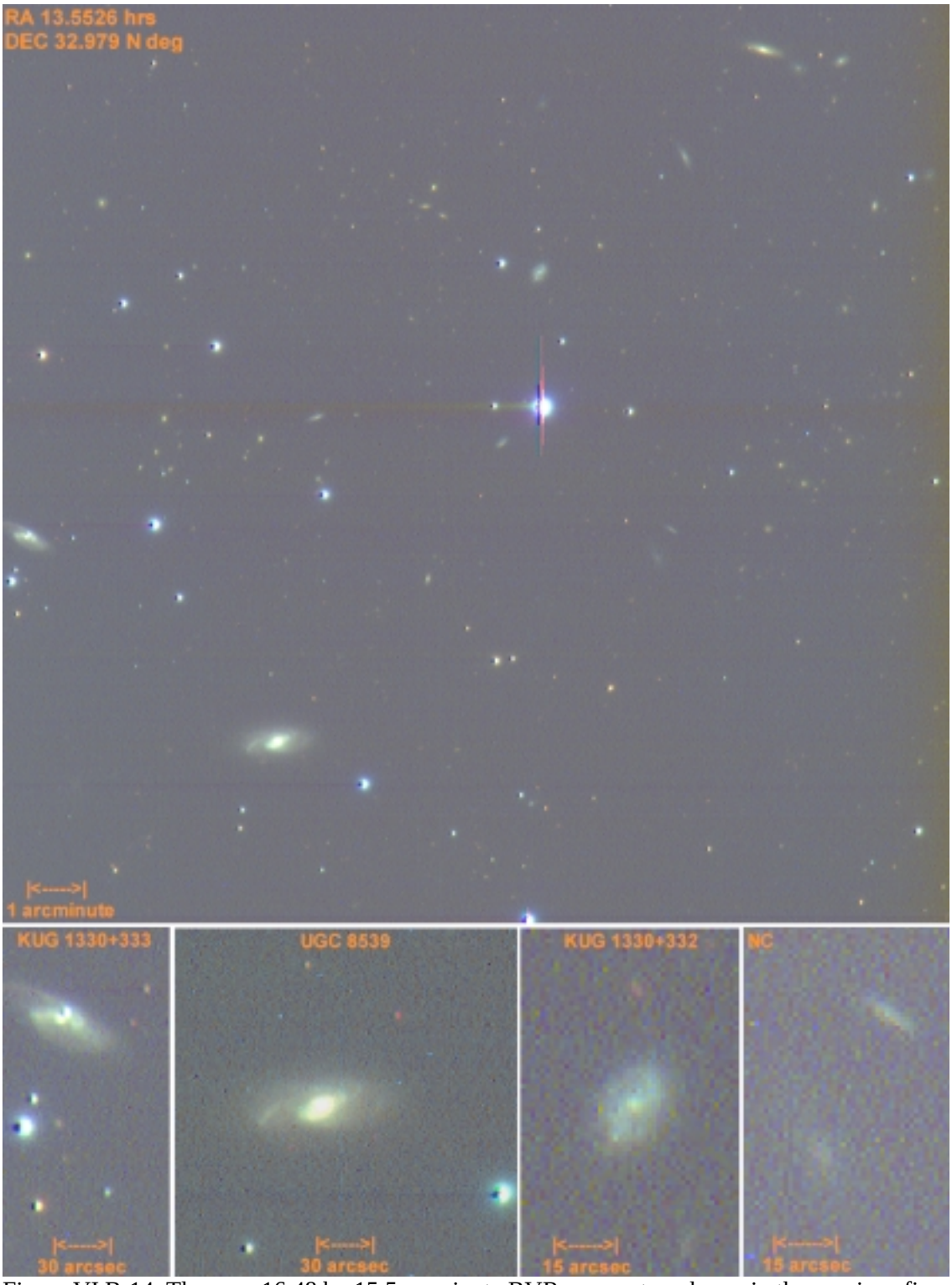

Figure VI.B-14. The same16.48 by 15.5 arcminute BVR segment as shown in the previous figure, but displayed with lower contrast to reveal structure in the brighter galaxies. From left to right, the insets show enlargements of three catalogued galaxies with V magnitudes of 15.5, 14.4, and 16.5 respectively. The fourth inset shows a faint spiral and LSB galaxy. Limiting magnitude at a 6.3 SN ratio is 22.0. West is up, North at left.

Figure VI.B-15. A BVR composite of a 30 arcminute long segment of the NASA-LMT survey strip in Canes Venatici. The BVR images were acquired with the NASA-LMT and PV 1K CCD through broadband filters in 1999 and 2000. Sample galaxies from this frame are shown in the next three figures. Limiting magnitude at a 6.3 SN ratio is ~22.0. West is up, North at left.

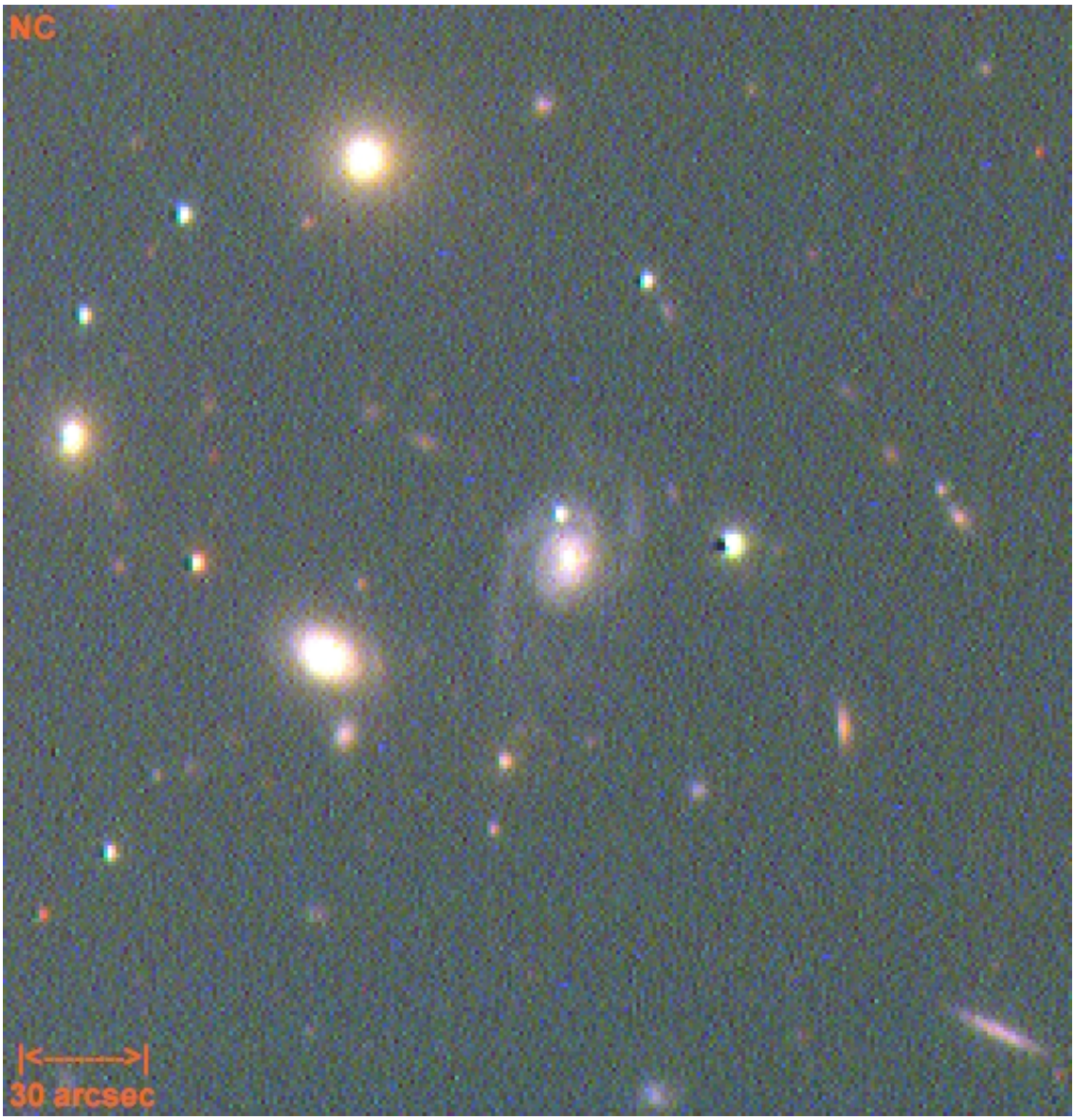

Figure VI.B-16. Sample un-catalogued (NC) galaxies in Canes Venatici from the previous figure (Figure VI.B-15). This approximately 4.5 by 4.5 arcminute field is centered at R.A. 13.887 hrs and Dec +33.090. Limiting magnitude at a 6.3 SN ratio is ~22.0. West is up, North at left.

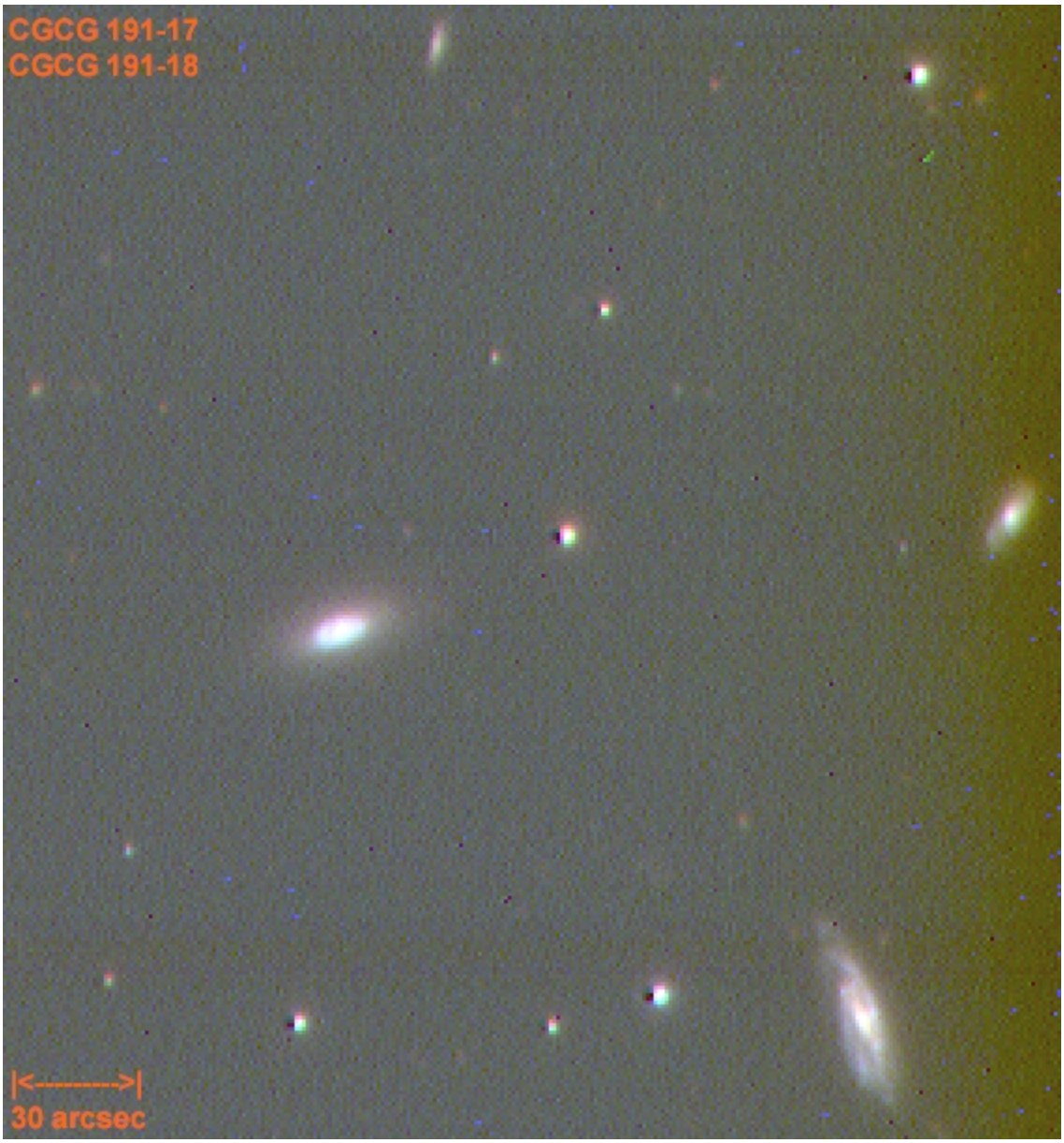

Figure VI.B-17. Sample galaxies in Canes Venatici from Figure VI.B-15. This approximately 4.5 by 4.5 arcminute field is centered at R.A. 13.918 hrs and Dec +33.903. The two brightest galaxies in the field have V magnitudes of 15.7 (upper) and 15.6 (lower). Limiting magnitude at a 6.3 SN ratio is ~22.0. West is up, North at left.

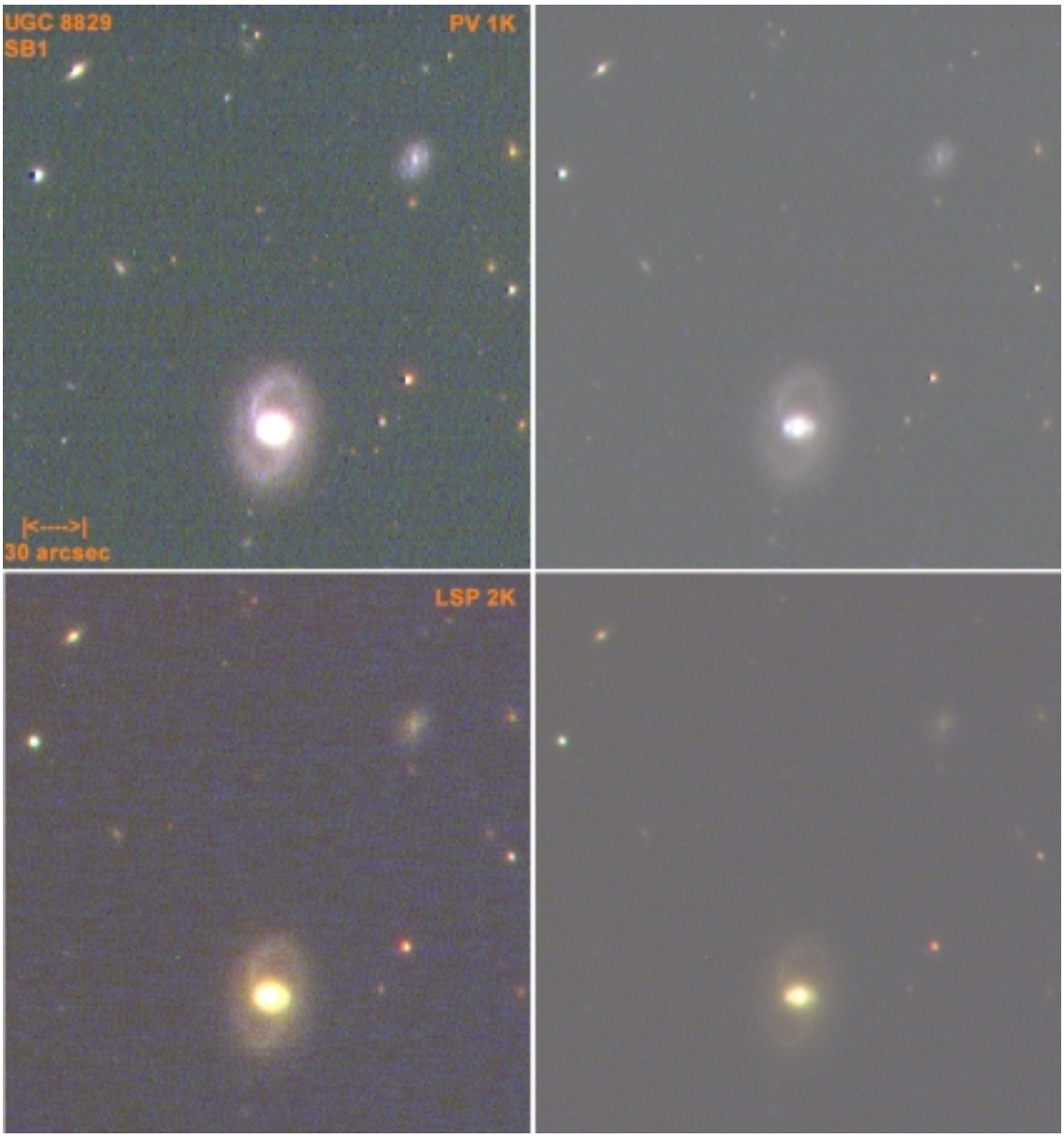

Figure VI.B-18. Sample galaxies in Canes Venatici from Figure VI.B-15 are shown in the upper frames at two different contrast levels to reveal alternately faint galaxies (left) and structure (right) in the SB.1 barred spiral galaxy UGC 8829. The lower two frames are similarly displayed, but were obtained with the LSP 2K CCD in 1996 and 1997. The yellow cast to the LSP data arises from its lack of B sensitivity. Despite the smaller 78 second exposure time for the PV 1K CCD relative to the 97.1 second exposure of the LSP 2K CCD, the former has noticeably higher sensitivity due to the higher quantum efficiency of its front illuminated CCD (Chapter IV). The brightest galaxy in the field (UGC 8829) has a V magnitude of 14.6. Limiting magnitude for the PV 1K CCD field at a 6.3 SN ratio is ~22.0. West is up, North at left.

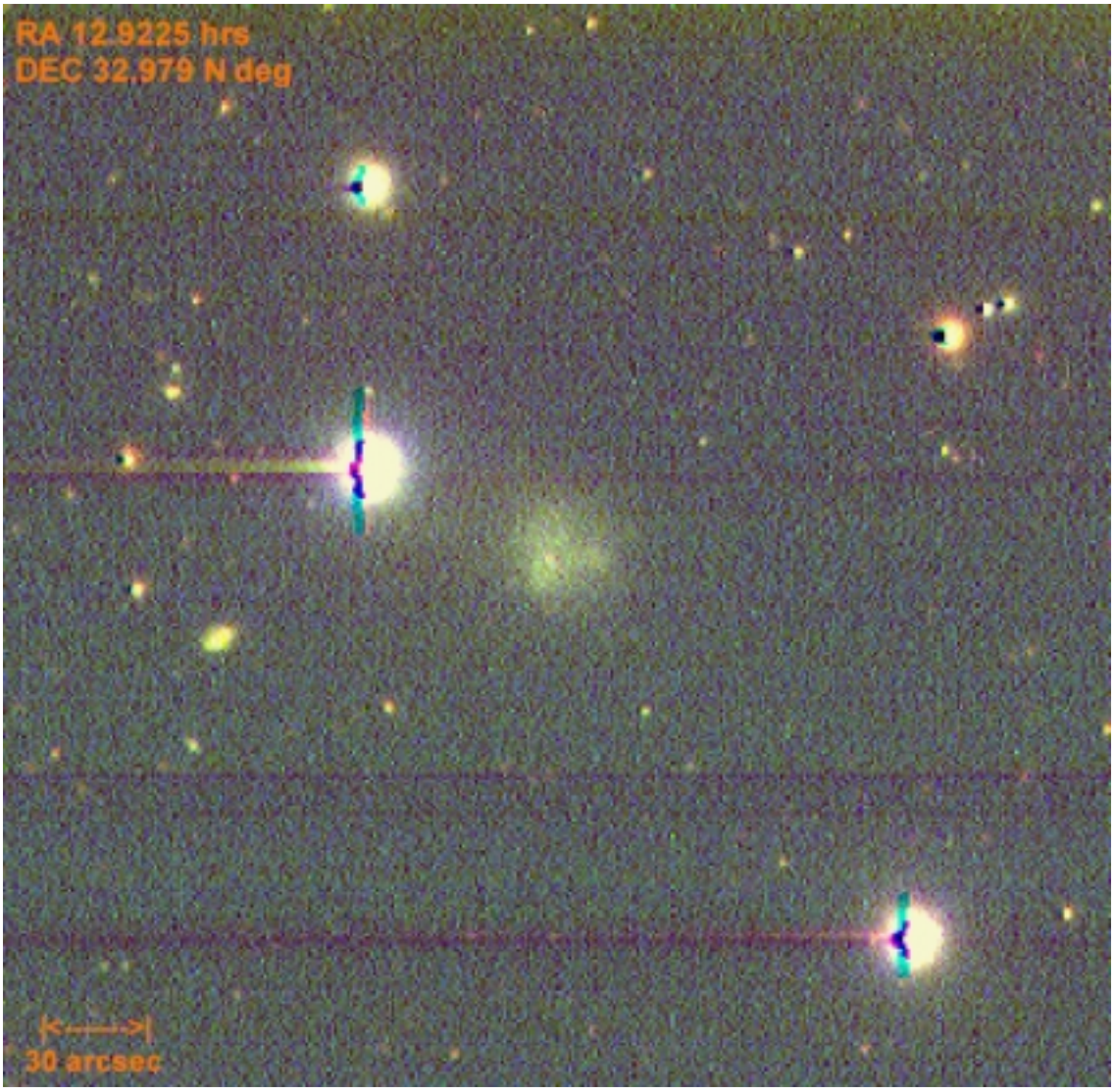

Figure VI.B-19. A BVR composite image from the NASA-LMT survey strip. The individual images were acquired with the NASA-LMT and PV 1K CCD through B,V, and R broadband filters in 1999 and 2000. This image shows an un-catalogued (NC) diffuse object in Canes Venatici which is possibly a planetary nebula based upon its greenish glow presumably due to forbidden oxygen emissions. Limiting magnitude at a 6.3 SN ratio is ~22.0. West is up, North at left.

NASA-LMT and Hubble Space Telescope Imagery of M57

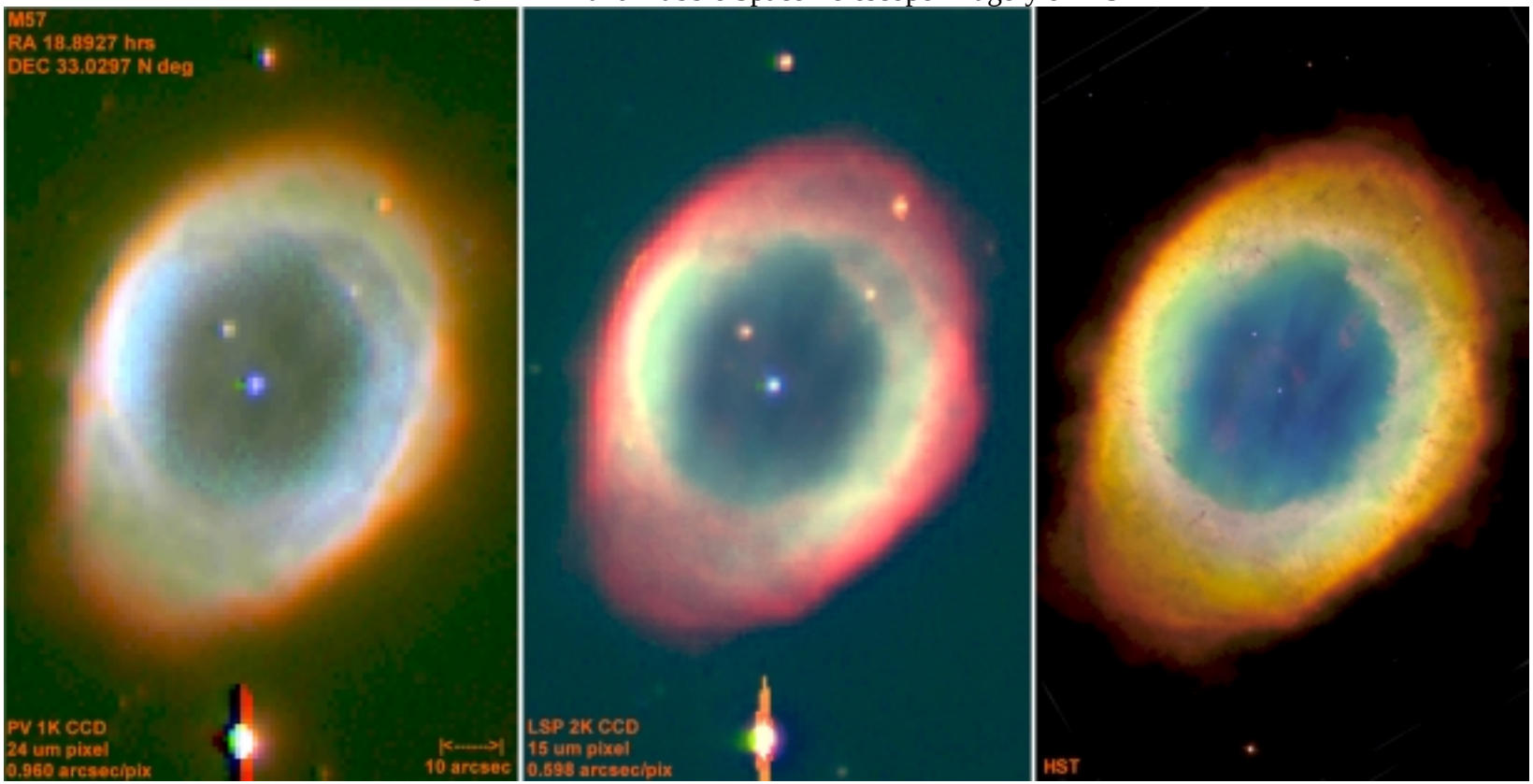

Figure VI.B-20. BVR composite views of the planetary nebula M57 (The Ring Nebula) in Lyrae. The first two images were acquired with the NASA-LMT using B, V, and R filters on separate nights. The left image was obtained with the 24 um pixel (0.960 arcsecond/pix) PV1K CCD, while the center was obtained with the higher resolution 15 um pixel (0.598 arcsecond/pix) LSP 2K CCD. The right image was acquired by HST and is shown as a high-resolution comparison. Although the 2K LSP CCD has higher resolution than the PV1K by virtue of its smaller pixels, it has very poor quantum efficiency in B. A PV1K B band image was re-sampled and substituted for use in the center composite to replicate the theoretical performance of a B sensitive 15 um CCD. Individual images were acquired throughout 1996-2000 NASA-LMT operations. Resolution for the LMT and HST images are 1.5 and 0.043 arcseconds FWHM respectively.

CONCLUSIONS

We have constructed a 3.0 m diameter Liquid Mirror Telescope and demonstrated capabilities comparable to conventional telescopes in terms of sensitivity, resolution, and utility for scientific inquest. The NASA-LMT has evolved from an initially rudimentary but intriguing performer at the NASA-JSC location, to a fully competent astronomical telescope during its six-year tenure at NODO. The techniques and instruments used for data acquisition have similarly evolved to yield increasingly valuable data products for both orbital object and astronomical research. Development continues in all areas in an effort to further refine the NASA-LMT system, to improve the image quality, and to expand research programs.

The LMT field is advancing rapidly as well. The 6.0 m diameter LZT, whose development was encouraged in part by the performance achievements of the NASA-LMT, will soon supplant it as the world's largest LMT. Its mirror container consisting of a machined membrane surface and space frame support will eliminate spin-casting and consequently the possible print through effect experienced with the NASA mirror (Chapter V). Because it is rigid and lightweight, this pioneering design is enabling the consideration of even larger liquid mirrors such as those planned for the Large Astronomical Mirror Array (LAMA) consisting of eighteen 10 m diameter liquid mirrors with an equivalent aperture diameter of 60 m and a 50% filling factor. This proposed array, intended primarily as a probe of large-scale structure, will employ adaptive optics, tracking secondary mirrors, and interferometric beam combining to enable diffraction

limited performance and 5 minute exposure times (Hickson PC). Figure C-1 illustrates the conceptual design while Figure C-2 demonstrates the expected performance relative to the 2.4 m HST and 8.0 m NGST (Next Generation Space Telescope) space-based platforms. At a cost of $50M, the LAMA project is more than an order of magnitude less expensive than comparable proposals using conventional glass mirrors. Figure C-3 shows a relative cost comparison between both existing and proposed conventional and liquid mirror telescopes.

In order to increase field coverage and thus further expand LMT flexibility, an off-axis LMT design allowing access 20 or more degrees from the zenith has been proposed by Wang et al. (1994). Such a system would further blur the distinction between the capabilities of LMTs and conventional telescopes. Less-costly hybrid designs like the Hobby-Eberly telescope (HET; Hill et al. 2000) which have features similar to an off-axis LMT (eg. inexpensive primary mirror, reduced infrastructure, limited pointing ability) are still not as cost-effective as LMTs, being still an order of magnitude more expensive for the equivalent aperture. The same is true of oven spun-cast conventional glass mirrors (Angel 1990) whose manufacture is simplified by the generation of a rough parabolic shape, but which still require costly figuring and polishing and elaborate support structures.

Until larger LMTs become operational, the NASA-LMT remains an operational test-bed for understanding the characteristics of the LMT system. The knowledge gleaned as development continues will not only benefit the research projects presently underway, but can also be used to benefit the design of other LMTs. We have predicted for example

Large Astronomical Mirror Array (LAMA) Conceptual Design

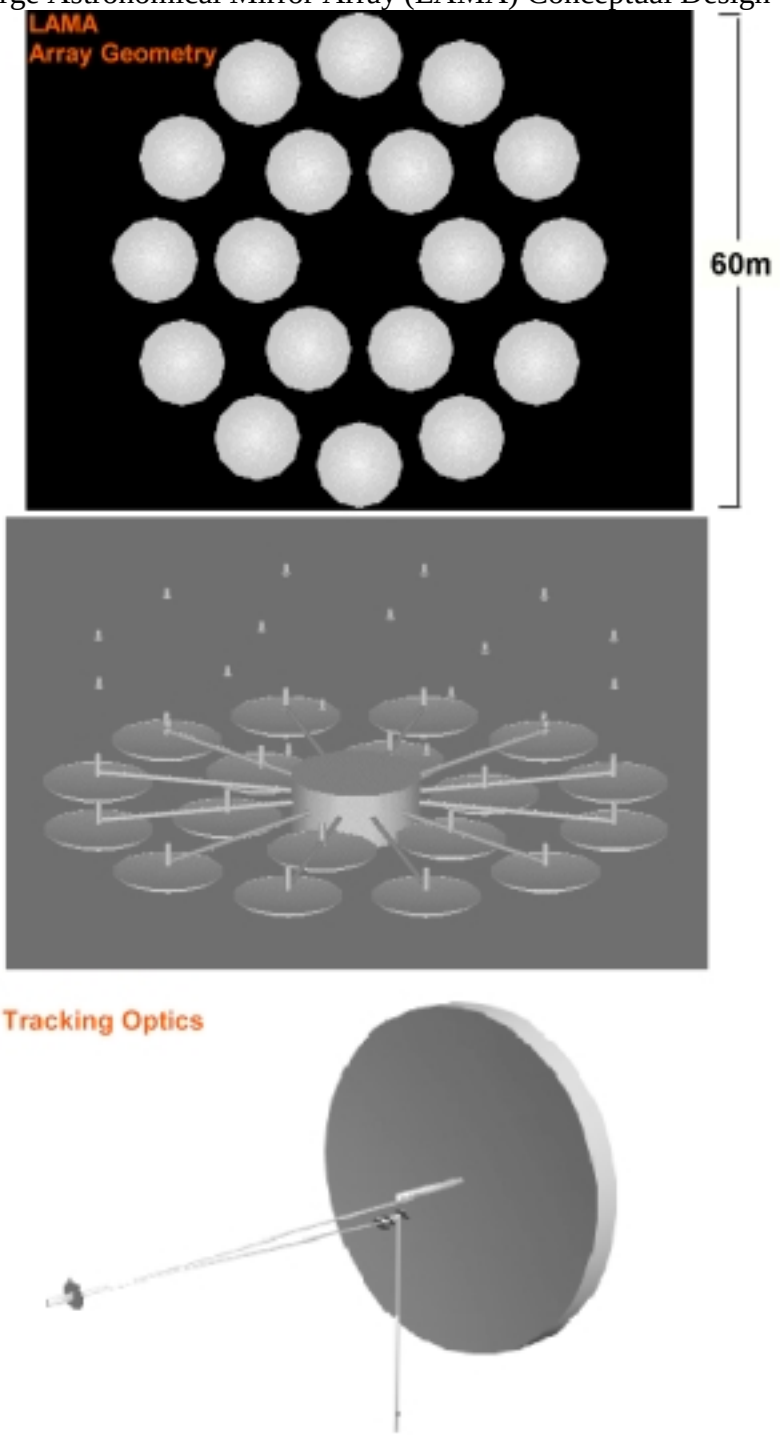

Figure C-1. The conceptual layout of the 60 m diameter Large Astronomical Mirror Array (LAMA). The eighteen individual 10 m diameter elements will possess tracking secondary mirrors and adaptive optics (AO) to yield exposure times of several minutes and diffraction limited performance. The indvidual element beams will be combined coherently using path length compensatation to yield a synthetic aperature with a 50% fill factor. (Images Credit: Paul Hickson)

Large Astronomical Mirror Array (LAMA) Theoretical Performance

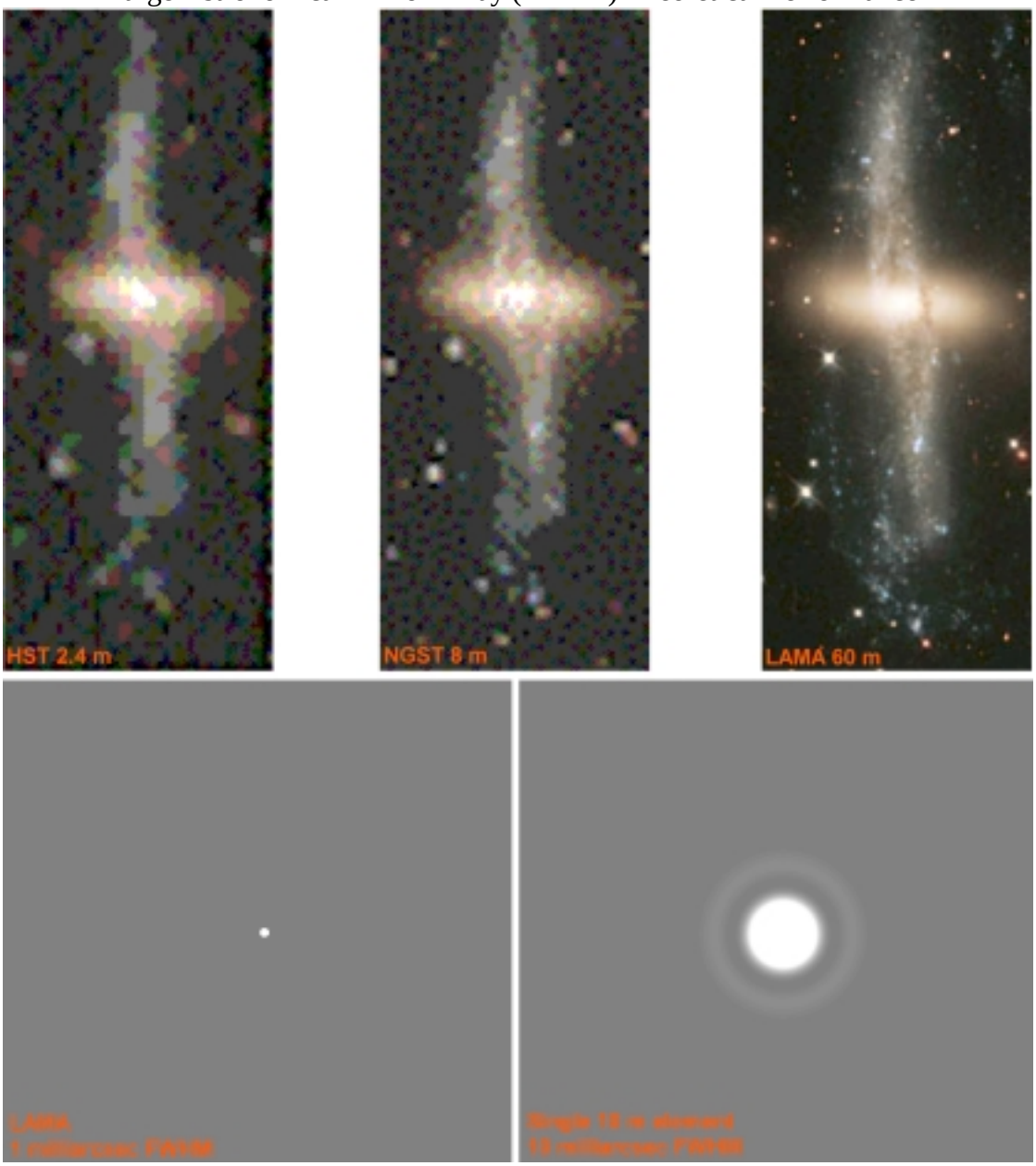

Figure C-2. The theoretical optical performance of the 60 m diameter Large Astronomical Mirror Array (LAMA). An artificially generated galaxy image is shown as imaged via the 2.4 m diameter Hubble Space Telescope (HST), the 8 m diameter Next Generation Space Telescope (NGST), and the LAMA. The lower figures show the Point Spread Function (PSF) for a point source as imaged by a single AO equipped 10 m diameter mirror (right) and the synthetic eighteen element array (left). An approximately 43 fold improvement in resolution relative to HST is possible (1 milliarcsecond FWHM). (Images Credit: Paul Hickson)

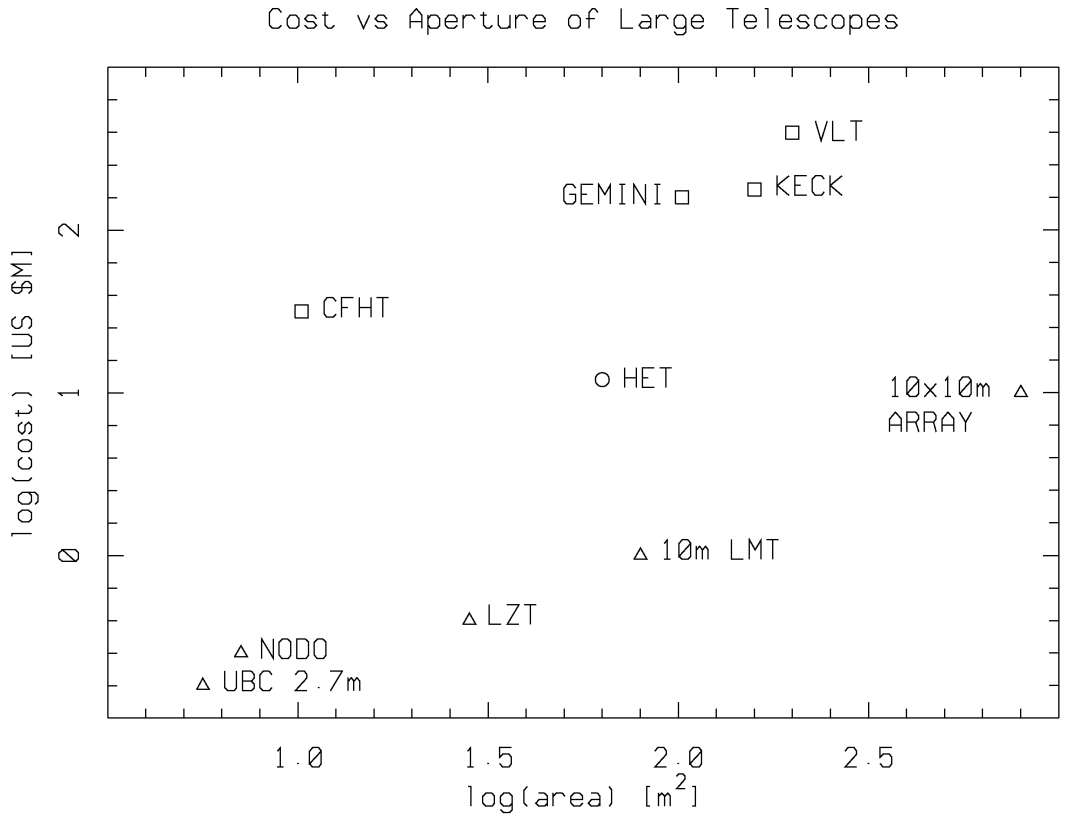

Figure C-3. A demonstration of the cost efficiency of LMTs relative to conventional instruments. At comparable apertures, the LMT is between one and two orders of magnitude less expensive than a conventional glass telescope. LMTs make ideal survey instruments for initially locating interesting objects or for large-scale structure research, whereas conventional instruments are well suited for more concentrated follow-up investigations of individual objects or smaller field areas. The two telescope forms are complimentary.

that turbulence may present a problem near the perimeter of the LZT as the airflow shifts from rolling vortices forming spiral waves to a possible chaotic disturbance of the Hg surface (Chapter III). Trials with baffling systems at NODO, may be helpful to LZT development if in fact there is a problem requiring mitigation. Experiments are also planned to evaluate improvements to the seeing environment in the vicinity of the mirror. A chilled fluid circulatory system is being considered to reduce convection in the volume of air beneath the liquid mirror. Mirror baffling and the convection suppression system should also reduce the mirror speed fluctuations which, as demonstrated in Chapter III, have an adverse affect on image resolution.

The efficacy of efforts to reduce waves and improve seeing, can be evaluated in real-time using the MCP intensified video camera in the off-axis configuration described in Chapter III, or more quantitatively through the use of an interferometer. A Smartt (Smartt 1975, 1979) point diffraction interferometer (PDI) has been discussed (Smartt and Hickson PC) as an alternative to the complex Scatter Plate interferometer employed by Borra et al. (1992). The interferometer would consist of a semi-transparent membrane with multiple small orifices which would be placed at the focal plane along with an imaging lens focused on the mirror coupled to either a high frame-rate CCD or one of the MCP intensified video cameras. As a star passed through the FOV, the plane wave portion of its wave front passing through the membrane would interfere with the spherical portion emanating from a given orifice and produce an interferogram of the mirror surface coupled with whatever seeing effects were present. Such a technique may be attempted after installation of the new 2K CCD in Fall 2000.

To support new observing programs, the new prime focus assembly, designed to enable remote alignment and detector and filter changes, can accommodate a variety of detectors in addition to the new PV 2K CCD and the 25 mm 3rd generation MCP intensified video camera presently in use. A new 40 mm 3rd generation MCP based camera is being investigated to expand the FOV for orbital object detection. The linear translation stage chosen to enable remote detector positioning, is of sufficient precision in terms positioning accuracy and motion to support an infrared detector in a mechanically drift-scanning configuration should one become available. The corrective optics are transmissive to 2 um where the reflectivity of mercury rises to 82 %, thus enabling modest expansion to the near IR.

Future NASA-LMT observational projects include analysis of the meteor event data acquired along with the orbital object observations. This comprehensive dataset with a limiting magnitude near 17.0 is unique since 3 m class telescopes are not extensively operated in a survey mode with the relatively high speed MCP intensified video detectors suitable for meteor detection. Screening is also planned of the present astronomical dataset for supernovas, flare stars, and for low surface brightness (LSB) galaxies whose surface brightness is below the sky background (McGaugh et al. 1995, O'Neil et al 1997, Impey and Bothun 1997). Since Hickson is already performing astrometry and photometry of every detected object within the survey, performing a search for these objects is now a matter of defining the appropriate selection criteria to filter the data. The multi-narrowband photometry can also yield radial metallicity profiles (Boroson et al. 1993) of galaxies with larger angular diameter (> ~20 arcsec) within the survey strip.

Recently a synergistic project combining elements of orbital detection and astronomy has been initiated at NODO. Data from Phase 2 of the multi-narrowband astronomical survey using the PV 2K CCD, as well as unfiltered white light data, will be screened for Near Earth Objects (NEOs) in an effort to characterize the population of asteroids and cometary bodies which may have the potential of catastrophically impacting the earth. Because these solar orbiting objects move at rates of typically 1 degree per day, they leave trails of only a few pixels in length during the relatively short drift-scan exposures of a fixed LMT. To differentiate between cosmic rays and NEO detections, a large CCD must be employed to give adequate exposure time. Figure C-4 shows an artificially generated trail which might be expected of a 1 degree/day, 19^{th} magnitude, 5 m diameter NEO at a distance of 500,000 km as captured by the NASA-LMT equipped with the drift-scanning PV 2K CCD with a 156 second exposure time. When this project begins towards the end of 2000, the NASA-LMT will have the highest detection sensitivity of any telescope involved in the NEO search. It is appropriate that the NASA-LMT has as its latest project a mission which integrates its capability as an astronomical survey instrument with its original design goal of studying the orbital object population - expanding its primary role of assessing the hazard posed to spacecraft to include the hazard posed to the earth itself.

NASA-LMT: Artificially Generated Near Earth Object (NEO) Signature

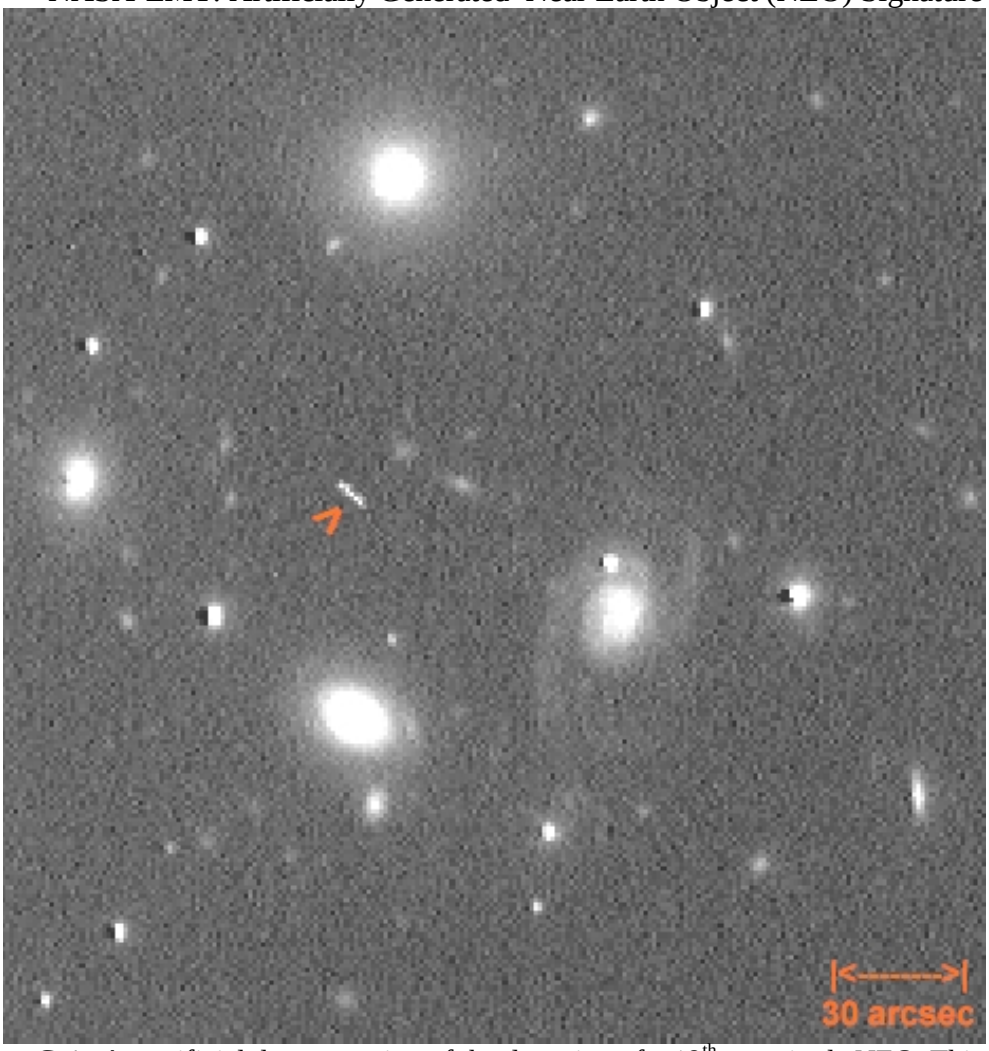

Figure C-4. An artificial demonstration of the detection of a 19th magnitude NEO. This 6 pixel long trail might be the signature of a 5 m diameter object at a 500,000 km distance, moving at 1 degree/day if imaged with the PV 2K CCD in a sidereal drift-scan mode with a 156 second exposure. If this R Band image (from Figure VI.B-15) had been acquired with the PV 2K CCD, rather than the PV 1K CCD, the limiting magnitude at a SN ratio of 6.3 would have been approximately 23.0. West is up, North at left.